A&A 661, A140 (2022)
https://doi.org/10.1051/0004-6361/202142971

Astronomy & Astrophysics

Observational constraints on the origin of the elements

IV. Standard composition of the Sun

Ekaterina Magg[1], Maria Bergemann[1,5], Aldo Serenelli[2,3,1], Manuel Bautista[4], Bertrand Plez[7], Ulrike Heiter[6], Jeffrey M. Gerber[1], Hans-Günter Ludwig[8], Sarbani Basu[9], Jason W. Ferguson[10], Helena Carvajal Gallego[11], Sébastien Gamrath[11], Patrick Palmeri[11], and Pascal Quinet[11,12]

[1] Max Planck Institute for Astronomy, Königstuhl 17, 69117 Heidelberg, Germany
e-mail: emagg@mpia-hd.mpg.de; bergemann@mpia-hd.mpg.de
[2] Institute of Space Sciences (ICE, CSIC), Carrer de Can Magrans S/N, 08193 Cerdanyola del Valles, Spain
[3] Institut d'Estudis Espacials de Catalunya (IEEC), Carrer Gran Capita 2, 08034 Barcelona, Spain
[4] Department of Physics, Western Michigan University, Kalamazoo, MI 49008, USA
[5] Niels Bohr International Academy, Niels Bohr Institute, University of Copenhagen, Blegdamsvej 17, 2100 Copenhagen, Denmark
[6] Observational Astrophysics, Department of Physics and Astronomy, Uppsala University, Box 516, 75120 Uppsala, Sweden
[7] LUPM, Univ. Montpellier, CNRS, Montpellier, France
[8] Landessternwarte – Zentrum für Astronomie der Universität Heidelberg, Königstuhl 12, 69117 Heidelberg, Germany
[9] Department of Astronomy, Yale University, PO Box 208101, New Haven, CT 06520-8101, USA
[10] Physics Department, Wichita State University, Wichita, KS 67260-0032, USA
[11] Physique Atomique et Astrophysique, Université de Mons, 7000 Mons, Belgium
[12] IPNAS, Université de Liège, 4000 Liège, Belgium

Received 21 December 2021 / Accepted 14 February 2022

ABSTRACT

Context. The chemical composition of the Sun is required in the context of various studies in astrophysics, among them in the calculation of standard solar models (SSMs) used to describe the evolution of the Sun from the pre-main-sequence to its present age.
Aims. In this work, we provide a critical re-analysis of the solar chemical abundances and corresponding SSMs.
Methods. For the photospheric values, we employed new high-quality solar observational data collected with the IAG facility, state-of-the art non-equilibrium modelling, new oscillator strengths, and different atmospheric models, including the MARCS model, along with averages based on Stagger and CO5BOLD 3D radiation-hydrodynamics simulations of stellar convection. We performed new calculations of oscillator strengths for transitions in O I and N I. For O I, which is a critical element with regard to the interior models, calculations were carried out using several independent methods. We investigated our results in comparison with the previous estimates.
Results. We find an unprecedented agreement between the new estimates of transition probabilities, thus supporting our revised solar oxygen abundance value. We also provide new estimates of the noble gas Ne abundance. In addition, we discuss the consistency of our photospheric measurements with meteoritic values, taking into account the systematic and correlated errors. Finally, we provide revised chemical abundances, leading to a new value proposed for the solar photospheric present-day metallicity of $Z/X = 0.0225$, which we then employed in SSM calculations. We find that the puzzling mismatch between the helioseismic constraints on the solar interior structure and the model can be resolved thanks to this new chemical composition.

Key words. Sun: abundances – stars: atmospheres – atomic data – line: formation – radiative transfer

1. Introduction

Research in modern astrophysics has demonstrated a growing interest in high-precision stellar abundance diagnostics as a source of accurate knowledge of the chemical composition of stars – relevant in studies of exoplanets (e.g. Bedell et al. 2018; Adibekyan 2019), asteroseismology and stellar structure (Nissen et al. 2017; Deal et al. 2020), and Galaxy evolution (Bensby et al. 2014; Bergemann et al. 2018; Schuler et al. 2021). Chemical abundances can only be determined from stellar spectra and, therefore, with the Sun set as the reference for any chemical diagnostics study, this effort requires self-consistent unbiased analyses of stellar and solar data. So far, however, accurate studies of solar abundances (Caffau et al. 2011; Asplund et al. 2021) have adopted methods and data that are conceptually different from those applied to large stellar samples. In particular, solar abundances are usually determined using full three-dimensional (3D) radiation transfer, without assuming local thermodynamic equilibrium (NLTE) methods employing spatially resolved solar spectra taken at different pointings across the solar disc (e.g. Amarsi et al. 2018; Bergemann et al. 2021). In addition, typically very weak atomic and molecular features across the entire range, from the optical to mid-IR at ∼1.5 µm, are used for solar analyses (such as the lines of OH, CN, CH, and NH, Amarsi et al. 2021), which are usually inapplicable for large samples of stars. In addition, full 3D NLTE calculations are computationally prohibitive and are currently not feasible for large stellar samples. Most large spectroscopic surveys, such as *Gaia*-ESO (Smiljanic et al. 2014), APOGEE (Majewski et al. 2017), and RAVE

(Steinmetz et al. 2020) still have to rely on spectroscopic models computed under simplifying assumptions of local thermodynamic equilibrium (LTE), one-dimensional (1D) geometry, and hydrostatic equilibrium, additionally adopting parameterisations for convective energy transport and turbulence. Thus far, GALAH (Buder et al. 2021) is the only survey that has adopted NLTE grids. In addition, spatially resolved spectra are not available for any other star than the Sun. Next-generation astronomical facilities, such as 4MOST and WEAVE, have stringent requirements on the quality of chemical abundance characterisation, but they will rely on medium-resolution spectral data.

In this work, we provide a new analysis of the solar chemical composition. The methodology was chosen to ensure that it is suitable for the analysis of any star (not only the Sun), with its very high-quality observations. We use the most up-to-date atomic and molecular data (Heiter et al. 2021, and updates described in Sect. 2.7), new NLTE model atoms (e.g. Semenova et al. 2020; Bergemann et al. 2021), and different solar model atmospheres (CO5BOLD and STAGGER) obtained by averaging 3D radiation-hydrodynamics (RHD) simulations of stellar convection. The latter is important in the view of the debate over the solar abundances between the two groups who use the STAGGER and CO5BOLD models. As the full 3D RHD computations are not applicable for the upcoming large spectroscopic surveys, given the complexity of the wide wavelength range abundance analysis. For this study, we chose to work with 1D and average 3D model atmospheres. We focus primarily on those chemical elements that are relevant in the calculation of the standard solar models (SSMs), that is C, N, O, Mg, Si, Ca Fe, and Ni. We also carefully revisit various observational constraints on the abundance of Ne, which cannot be determined from the solar photospheric spectra. However, independent measurements based on the solar wind and corona are available (Bochsler 2007). We selected atomic spectral lines that can also be used to derive abundances from medium resolution spectral data. Here, we also discuss the photospheric measurements of O (e.g. Bochsler 2007; Laming et al. 2017) in the context of the Ne/O ratio. We compare our results with previous estimates in the literature, as well as with those based on the analysis of the B-type stars in the solar neighbourhood (Nieva & Simón-Díaz 2011; Nieva & Przybilla 2012).

The paper is organised as follows. In Sect. 2, we describe the observational material and the solar model atmospheres employed in this work. We summarise the key details of NLTE model atoms, statistical equilibrium and synthetic spectra calculations, and the input line list. In Sect. 3, we present our new solar abundance estimates and compare them with the literature. We close with the analysis of the new chemical composition in the SSM calculations in Sect. 3.4 and draw our conclusions in Sect. 4.

2. Analysis

2.1. Observed data

We used a high-quality, high-resolution ($R = \lambda/\Delta\lambda \approx 700\,000$) solar flux spectrum obtained with the FTS instrument at the Institut für Astrophysik, Göttingen (hereafter IAG data, Reiners et al. 2016). In Bergemann et al. (2021), we investigated the differences between solar abundance estimates obtained using the IAG data, the KPNO FTS solar flux atlas, the data acquired with the Hinode space based facility, and several other datasets. We found that in some cases, non-negligible differences arise due to the use of different solar atlases (see also Caffau et al. 2008). However, the differences are primarily associated with instrumental artefacts and effects of the data reduction. As a consequence, part of the discrepancies between the solar abundance estimates (e.g. Asplund et al. 2021; Caffau et al. 2011) arguably arise because of the latter aspect, since they focus on weak features that are particularly sensitive to the details of the continuum placement.

In this work, we do not restrict the analysis to the weakest lines, thus, we also include other spectral lines that will be accessible with next generation facilities such as 4MOST and WEAVE. As we will show in Sect. 3, we do not detect any significant systematic biases in abundances, caused by using lines across a broad range of equivalent widths, as long as the atomic data employed in the analysis are of a sufficiently high quality.

2.2. Model atmospheres

We made use of three different sources of solar atmospheric models: the MARCS model (Gustafsson et al. 2008), the STAGGER model (Magic et al. 2013a,b), and the CO5BOLD model (Freytag et al. 2012). The physical properties of the MARCS model atmosphere code are extensively described in Gustafsson et al. (2008). It is a 1D LTE model atmosphere computed under the assumption of hydrostatic equilibrium and with convective energy transfer treated according to the mixing length theory formalism of Henyey et al. (1965). The mixing length was set to 1.5 and microturbulence to $1\,\mathrm{km\,s^{-1}}$. The code relies on opacities computed using the Uppsala opacity package, which was updated to include comprehensive bound-bound and bound-free transitions in all relevant absorbers in FGK atmospheres, as well as lines for about 20 important molecular species. In total, over 500 molecules are included in the equation of state calculations.

Here, we use the averages of these simulations[1], constructed by spatial (over surfaces of equal optical depth) and temporal averaging of the simulation cubes, as described in Bergemann et al. (2012). These averages are known as ⟨3D⟩ model atmospheres. To represent the original 3D velocity field in the simulation cubes, we included a depth-dependent velocity profile in the form of a microturbulence with a value of one standard deviation of the 3D velocity components, as suggested in Uitenbroek & Criscuoli (2011). The opacities and the equation of state used in the RHD calculations are described in Magic et al. (2013a,b).

The mean CO5BOLD model (see Freytag et al. 2012, for a description of the code) was obtained by horizontal (on $\tau_{\mathrm{Rosseland}}$ iso-surfaces, first temperature moment) averaging of data blocks from a solar model simulation (internal identifier `d3gt57g44msc600`). The model is part of the ongoing extensive efforts for the development of the `CIFIST` 3D model atmosphere grid (Ludwig et al. 2009; Tremblay et al. 2013). The 3D model uses $250 \times 250 \times 207$ grid points, with an equidistant grid spacing of 32 km in the two horizontal directions and a non-equidistant grid spacing in the vertical direction between 10 and 15 km, giving a total extension of $8.0 \times 8.0 \times 2.3\,\mathrm{Mm}^3$. The wavelength dependence of the radiative transfer was represented with 12 opacity bins. A comparison of the temperature structures of the STAGGER and CO5BOLD model atmospheres used in this study is presented in Fig. 1.

[1] https://staggergrid.wordpress.com/mean-3d/

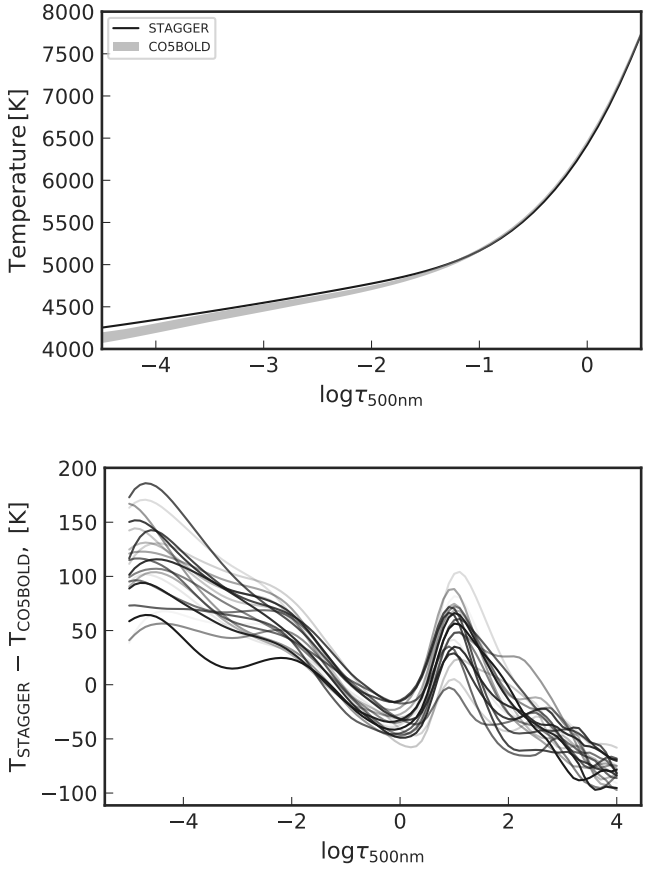

Fig. 1. Comparison of the temperature structure of the model atmosphere simulations used in this study. *Top panel*: temperature structure of STAGGER and CO5BOLD model atmospheres. Gray area depicts variations among temporarily resolved snapshots in CO5BOLD simulations. *Bottom panel*: absolute difference in temperature structure of STAGGER and CO5BOLD model atmospheres. Each line corresponds to a temporarily resolved snapshot of CO5BOLD simulations. See Sect. 2.3 for details.

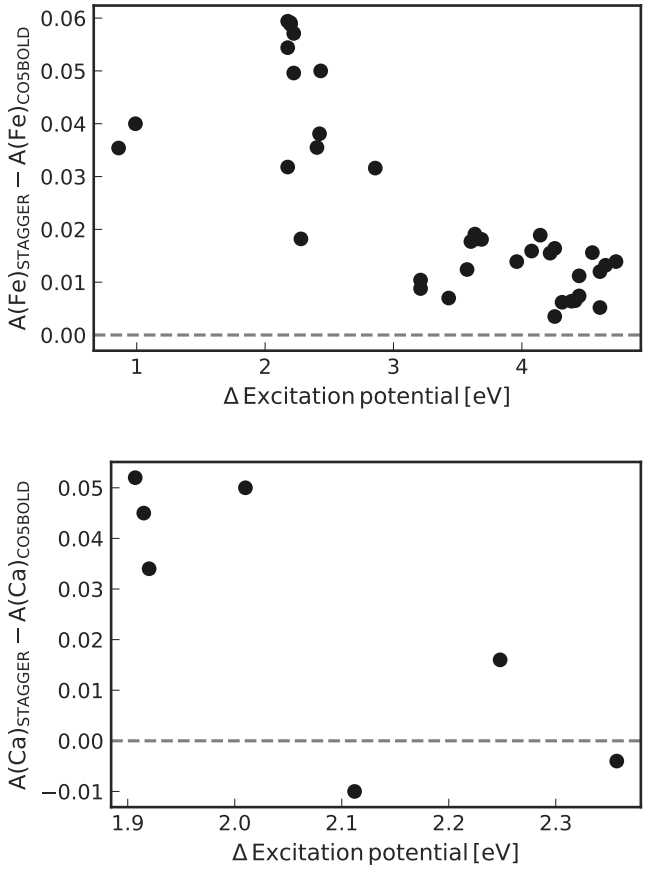

Fig. 2. Influence of model atmosphere choice on obtained abundances. *Top panel*: predicted difference in Fe abundance computed with STAGGER and CO5BOLD model atmospheres as a function of lower level excitation potential for Fe I lines. *Bottom panel*: predicted difference in Ca abundance computed with STAGGER and CO5BOLD model atmospheres as a function of difference in lower level excitation potential for Ca I lines. See Sect. 2.3 for details.

2.3. Comparative analysis of CO5BOLD and STAGGER results

To test how the choice of model atmosphere affects the derived abundances, we computed the curve-of-growth (COG) for each diagnostic line of each chemical element using the CO5BOLD and STAGGER solar atmospheric models. Since there is no consensus thus far on how to average the 3D velocity field, we chose to include velocity as a form of microturbulence and we set it to 1 km s^{-1} in both model atmospheres. By comparing the COGs, we estimated the difference in abundance for each chemical element. It is known that NLTE radiative transfer is much less sensitive to the temperature structure of the model atmosphere of Bergemann et al. (2012); this because the populations are significantly affected by the non-local radiation field. Thus, we performed the comparison in NLTE whenever possible. This predicted difference is provided in Table 4 and we refer to it later in the discussion when comparing abundances derived using the CO5BOLD and STAGGER models.

Overall, the STAGGER model atmosphere is hotter than CO5BOLD (Fig. 1), with a negligible difference around the optical depth $\log \tau_{500\,\mathrm{nm}} = 0$, but up to 150 K at larger optical depths. Figure 2 shows that Fe I lines with lower levels of excitation potential, $E_{\mathrm{low}} \lesssim 2.5$ eV, are very sensitive to the temperature structure of the atmosphere, and the abundances inferred from these features may differ by up to +0.06 dex depending on the detailed structure of the ⟨3D⟩ model. In contrast, the Fe abundances derived from Fe I lines with higher E_{low} values change by less than 0.02 dex. This is as expected, and confirms previous NLTE results (e.g. Bergemann et al. 2012). Therefore, in this work, we chose to include only Fe I lines with high excitation potential, $E_{\mathrm{low}} \geq 2.5$ eV, in the abundance analysis.

Also, the lines of Ca I show a significant sensitivity to the structure of the models. The majority of diagnostic Ca I lines in our linelist arise from levels with intermediate excitation potential, $E_{\mathrm{low}} \approx 2.5$ eV. As Fig. 2 demonstrates, the strong Ca I lines at 6471 and 6499 Å (with the smallest energy level differences) have the largest difference in abundance when modelled with the CO5BOLD and STAGGER model, up to 0.05 dex. Since we do not currently have a robust evidence in favour of either of these 3D RHD simulations, we opted to include all Ca lines in the analysis, given the much smaller number of diagnostic features of Ca I available for the abundance analysis compared to Fe I. The lines of all other elements (shown in Table 4), appear to be almost unaffected by the differences between CO5BOLD and STAGGER models. Therefore, we used all available diagnostic lines in the calculations, without imposing any cuts on their atomic parameters.

2.4. Abundance analysis

The analysis of spectral lines is a two-step procedure. First, we computed NLTE atomic level populations for each of the NLTE elements described in Sect. 2.5, using a code that simultaneously solves the radiative transfer and statistical equilibrium equations. Second, we adopted the NLTE populations into a spectrum synthesis code to compute model spectra for all diagnostic lines of the selected chemical elements, taking all atomic and molecular blends self-consistently into account. The abundances are then derived by comparing the grid of model spectra with the data, employing standard χ^2 minimisation. We verified, based on mock lower-resolution observed data, that the abundances are not affected by reducing the resolving power and signal-to-noise ratio (S/N) of the spectra by more than 0.03 dex.

For the NLTE calculations, we used the MULTI2.3 code (Carlsson 1986), which is based on the method of accelerated lambda iteration (or ALI) and solves the radiative transfer equation using the long characteristics solver. The code was updated, as described in Bergemann et al. (2019) and Gallagher et al. (2020). The atomic populations calculated by MULTI2.3 were then used with the spectrum synthesis code Turbospectrum (Plez 2012), which can self-consistently treat blends and compute a full spectrum while including all species simultaneously.

2.5. NLTE model atoms

New atomic models are available for five chemical elements in our list. We describe them briefly below. The Grotrian diagrams are illustrated in Fig. 3.

The model atoms of O and Ni are both taken from Bergemann et al. (2021). In short, the O model includes 122 energy states of O I and O II, coupled by radiative and collision-induced transitions. Radiative data were adopted from the Kurucz[2] database and supplemented with new photo-ionisation cross-sections for O I states computed using the R-matrix method (Berrington et al. 1995). This method was also used to derive new data for electron-impact transitions. Then, H-induced inelastic processes were computed using the OH molecule, employing the multi-reference configuration interaction (MRCI) method and the collisional dynamics description presented by Belyaev et al. (2019). The model atom of Ni primarily relies on the same sources of radiative data (NIST[3], Kurucz), whereas the collisional data were calculated using the standard formulae presented in van Regemorter (1962), Seaton (1962), Drawin (1968).

The Mg model atom is described in detail in Zhao et al. (1998) and in Mashonkina (2013), and slightly updated in Bergemann et al. (2017). The model includes 86 energy states, of which 85 represent Mg I, closed by Mg II. Radiative transitions were adopted from the Opacity Project (The Opacity Project Team 1995), with 453 of these transitions connecting the energy levels in Mg I and for 65 states bound-free transition included. The collisional data were taken from Mauas et al. (1988) and Zhao et al. (1998) for $e^- + Mg$ collisions, and Barklem et al. (2012) was the main source for H I impact excitation and charge exchange processes. Electron-impact ionisation rate coefficients were computed using the Seaton (1962) formula.

The Fe model is described in detail in Bergemann et al. (2012) and recently updated by Semenova et al. (2020). In particular, Fe I has probably the most complex system of energy levels of all species in the periodic table, thus, representing them in a model is a major numerical challenge. In the Kurucz database, over 37 000 energy levels and over 6 million transitions are available. The model we employ in this work contains 637 Fe I states and 58 Fe II states, which are connected via 19 267 radiative bound-bound transitions. Fine-structure levels of Fe I are included up to ∼7 eV. We also included very high-excitation energy levels of Fe I, using the super-levels and super-lines following Bergemann et al. (2012). The uppermost energy state in Fe I (a super-level) is thus located at 7.88 eV, only 0.07 eV from the first ionisation threshold (7.95 eV), representing the ground state (term) of Fe II. We note that it is common to use fine-structure levels for Fe II, however, all ionisation photo-ionisation cross-sections and charge transfer rates are defined for LS states (not for fine structure levels). We tested whether using the actual ionisation thresholds for Fe II levels or representing them as terms has an impact on our results, and we found that the difference in abundance space was only 0.01 dex; this is negligible compared to other sources of error in the analysis. We note that the NIST database is very incomplete with regard to the Fe I structure above 7.5 eV. We therefore also tested more compact atomic models of Fe, devoid of energy levels higher than 7.50 eV in the Fe I system, and we found that using more compact models does not affect the abundances determined from Fe I lines by more than 0.01 dex.

Bound-free radiative cross-sections were taken from Bautista et al. (2017), whereas the rates of transitions caused by collisions with e^- and H atoms were computed using the new quantum-mechanical estimates of the cross-sections by Bautista et al. (2017) and Barklem (2018), respectively. The photo-ionisation cross-sections were tabulated in a fine energy grid, to resolve resonances. This is particularly important because Fe I (and other Fe-group species) react very sensitively to the radiation field, and over-ionisation is indeed the main process behind non-negligible NLTE effects, especially at low metallicity (Bergemann & Nordlander 2014; Amarsi et al. 2016).

The atomic model of Si is based on the model presented by Bergemann et al. (2013), however, with important updates to the radiative and collisional part of the atom. The f-values and damping constants for the Si I lines were substituted by the most recent data available in the Kurucz database[4]. The rate coefficients that describe the processes in inelastic collisions between Si I and H atoms were adopted from Belyaev et al. (2014) and from the database from Paul Barklem[5]. The rate coefficients describing the charge transfer and mutual neutralisation reactions were adopted from Belyaev et al. (2014).

2.6. New oscillator strengths for N and O

To compute the new values of the oscillator strengths, we adopted various independent approaches.

For the O I lines, we used the pseudo-relativistic Hartree-Fock method, originally introduced by Cowan (1981) and modified to account for core-polarisation effects (HFR+CPOL). This is described, for instance, by Quinet et al. (1999, 2002). We also used the fully relativistic multiconfiguration Dirac-Hartree-Fock (MCDHF) approach developed by Grant (2007) and Froese Fischer et al. (2016) with the latest version of GRASP (General Relativistic Atomic Structure Program), known as

[2] http://kurucz.harvard.edu/
[3] https://physics.nist.gov
[4] http://kurucz.harvard.edu/atoms/1400/, based on Kurucz 2016 calculations.
[5] https://github.com/barklem

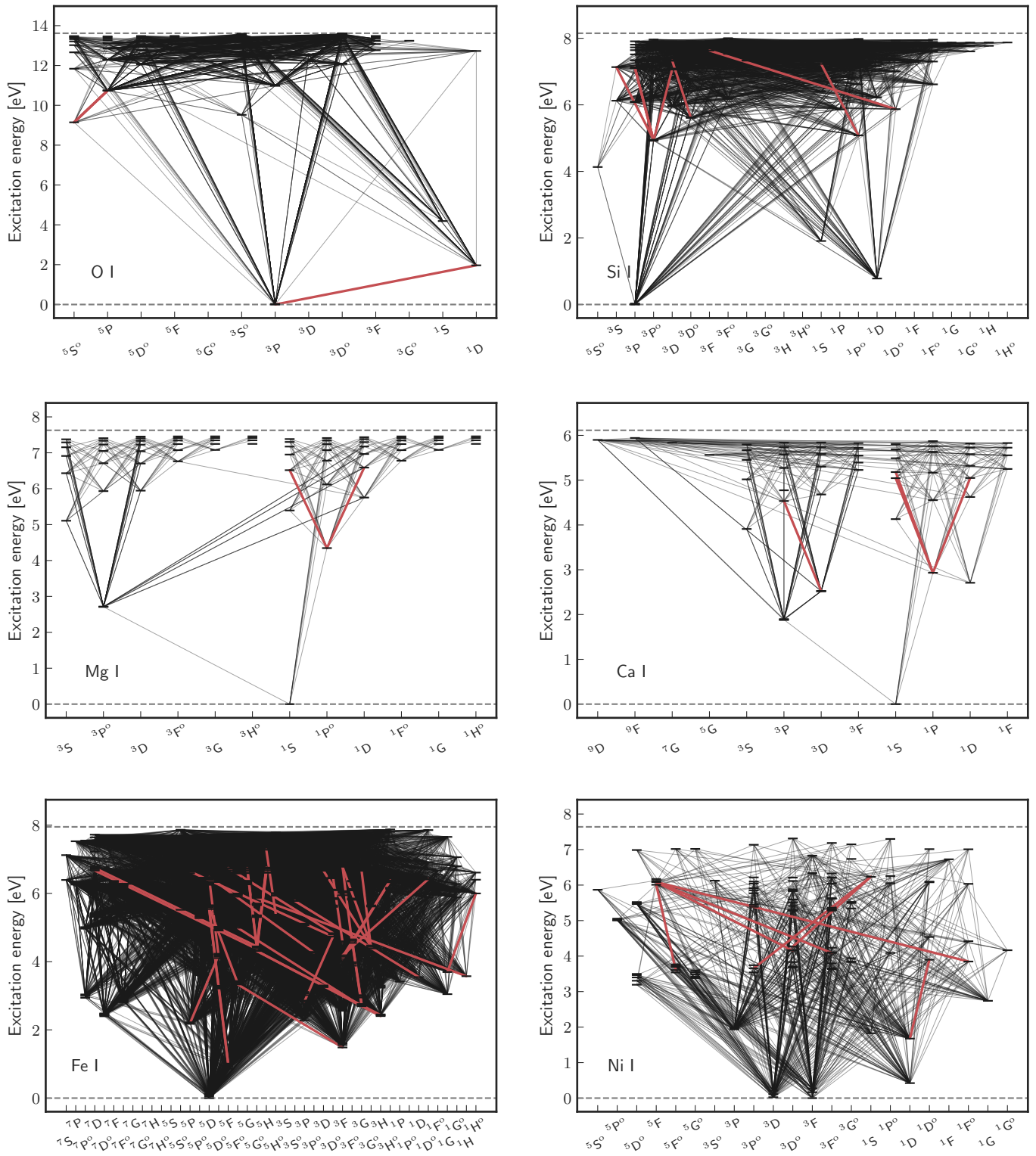

Fig. 3. Grotrian diagrams for chemical elements treated in NLTE. Energy states are depicted with horizontal dashes and connecting bound-bound radiative transitions are shown with black lines. Red lines correspond to diagnostic transitions used in abundance analysis. Only energy levels following L-S coupling are shown.

GRASP2018 (Froese Fischer et al. 2019). In our HFR+CPOL calculations, the valence-valence interactions were considered among a set of configurations including $2p^4$, $2p^3$ *nl* (with *nl* up to 6h) and all single and double excitations from 2s, 2p to 3s, 3p, 3d orbitals, while the core-valence correlations were modelled with a core-polarisation potential corresponding to a He-like O VII ionic core with a dipole polarizability $\alpha_d = 0.0026\,a_0^3$ (Johnson et al. 1983) and a cut-off radius of $r_c = 0.198\,a_0$. The latter value corresponds to the calculated HFR value of $\langle r \rangle$ of the outermost core orbital (1s). For the MCDHF calculations, we adopted a physical model in which valence-valence correlations are considered by means of single and double excitations

Table 1. Atomic parameters of diagnostic spectral lines of C I, N I, O I, Mg I, Si I, Si II, Ca I, Ni I, and Ni II.

λ [Å]	E_{low} [eV]	E_{up} [eV]	log gf	vdW [a]	Ref. [b] f-val.	Ref. [c] vdW
C I						
5052.145	7.685	10.138	−1.36 ± 0.04	−7.310	1	4
6587.610	8.537	10.419	−1.05 ± 0.04	1953.319	1	1
7113.171	8.647	10.390	−0.94 ± 0.04	1858.314	1	1
N I						
8629.235	10.690	12.126	0.006 ± 0.07	575.234	2	1
8683.403	10.330	11.757	0.162 ± 0.04	480.231	2	1
O I						
6300.304	0.000	1.967	−9.72 ± 0.08	–	3	2
7771.940	9.146	10.741	0.350 ± 0.02	453.234	2	1
7774.170	9.146	10.741	0.204 ± 0.02	453.234	2	1
7775.390	9.146	10.740	−0.019 ± 0.02	453.234	2	1
Mg I						
5528.405	4.346	6.588	−0.547 ± 0.02	1461.312	4	1
5711.088	4.346	6.516	−1.742 ± 0.05	1860.100	4	3
Si I						
5645.611	4.930	7.125	−2.067 ± 0.03	−7.29	5	4
5684.484	4.954	7.134	−1.607 ± 0.05	−7.30	5	4
5690.425	4.930	7.108	−1.802 ± 0.05	1770.220	5	1
5701.105	4.930	7.104	−1.981 ± 0.05	1770.220	5	1
5772.146	5.082	7.223	−1.643 ± 0.03	−7.350	5	4
5793.073	4.930	7.069	−1.894 ± 0.1	1700.230	5	1
7034.900	5.871	7.633	−0.78	−7.13	6	4
7226.208	5.614	7.329	−1.41	−7.32	6	4
Si II						
6371.372	8.121	10.067	−0.120 ± 0.001	−7.69	5	4
Ca I						
5260.387	2.521	4.878	−1.719 ± 0.02	421.260	7	1
5512.980	2.933	5.181	−0.464 ± 0.02	−7.316	8	4
5867.562	2.933	5.045	−1.570 ± 0.04	−7.460	8	4
6166.439	2.521	4.531	−1.142 ± 0.02	976.257	7	1
6455.598	2.523	4.443	−1.340 ± 0.04	365.241	8	1
6471.662	2.526	4.441	−0.686 ± 0.02	365.241	7	1
6499.650	2.523	4.430	−0.818 ± 0.02	364.239	7	1
Ni I						
4740.165	3.480	6.095	−1.72	844.281	9	1
4811.983	3.658	6.234	−1.45	−7.75	10	4
4814.598	3.597	6.172	−1.63	743.236	9	1
4976.135	3.606	6.097	−1.26	843.282	9	1
5157.980	3.606	6.009	−1.51	691.236	9	1
5537.106	3.847	6.086	−2.22	695.216	9	1
6176.812	4.088	6.095	−0.26	826.284	9	1
6204.604	4.088	6.086	−1.08	719.247	9	1
6223.984	4.105	6.097	−0.91	827.283	9	1
6414.587	4.154	6.086	−1.16	721.249	9	1
Ni II						
6378.250	4.154	6.097	−0.82	825.283	9	1

Notes. [a]Van der Waals broadening parameter, see text. [b]*References*: (1) Li et al. (2021); (2) this work; (3) Storey & Zeippen (2000); (4) Pehlivan Rhodin et al. (2017); (5) H. Hartman (in prep., and priv. comm.); (6) Garz (1973) renormalised using O'Brian & Lawler (1991); (7) Smith & Raggett (1981); (8) Smith (1988); (9) Wood et al. (2014); (10) Johansson et al. (2003). [c]*References*: (1) Barklem et al. (2000); (2) Unsöld (1955); (3) P. Barklem (priv. comm.); (4) Anstee & O'Mara (1991, 1995).

Table 2. Atomic parameters of diagnostic Fe lines.

λ [Å]	E_{low} [eV]	E_{up} [eV]	log gf	vdW [a]	Ref. [b] f-val.	Ref. [c] vdW
Fe I						
5242.491	3.634	5.999	−0.967 ± 0.046	361.248	1	1
5365.399	3.573	5.883	−1.020 ± 0.041	283.261	1	1
5379.574	3.695	5.999	−1.514 ± 0.046	363.249	1	1
5398.279	4.446	6.742	−0.630 ± 0.060	993.280	2	1
5543.936	4.218	6.453	−1.040 ± 0.050	742.238	2	1
5560.212	4.435	6.664	−1.090 ± 0.050	895.278	2	1
5638.262	4.220	6.419	−0.720 ± 0.020	730.235	3	1
5661.346	4.284	6.474	−1.765 ± 0.041	765.209	4	1
5679.023	4.652	6.835	−0.820 ± 0.050	1106.291	2	1
5731.762	4.256	6.419	−1.200 ± 0.050	727.232	2	1
5741.848	4.256	6.415	−1.672 ± 0.097	725.232	1	1
5855.077	4.608	6.725	−1.478 ± 0.041	962.279	4	1
5905.672	4.652	6.751	−0.690 ± 0.050	994.282	2	1
5930.180	4.652	6.742	−0.230	983.281	5	1
6027.051	4.076	6.132	−1.089 ± 0.051	380.250	1	1
6056.005	4.733	6.780	−0.320 ± 0.030	1029.286	3	1
6093.644	4.608	6.642	−1.400 ± 0.080	866.274	2	1
6165.360	4.143	6.153	−1.473 ± 0.051	380.250	1	1
6187.990	3.943	5.946	−1.620 ± 0.060	903.244	2	1
6270.225	2.858	4.835	−2.470 ± 0.059	350.249	8	1
Fe II						
5234.625	3.221	5.589	−2.180	180.249	10	2
5325.553	3.221	5.549	−3.160	179.252	10	2
5425.257	3.199	5.484	−3.220	178.255	10	2
6084.111	3.199	5.237	−3.881	173.223	11	2
6456.383	3.903	5.823	−2.185	185.276	11	2

Notes. [a]Van der Waals broadening parameter, see text. [b]*References*: (1) O'Brian et al. (1991); (2) May et al. (1974); (3) Ruffoni et al. (2014); (4) Bard & Kock (1994); (5) Wolnik et al. (1971) renormalised to Fuhr et al. (1988); (6) Average of Bard et al. (1991), Blackwell et al. (1982a), and O'Brian et al. (1991); (7) Blackwell et al. (1982a); (8) Average of Bard et al. (1991) and O'Brian et al. (1991); (9) Average of Blackwell et al. (1982b) and O'Brian et al. (1991); (10) Meléndez & Barbuy (2009); (11) Raassen & Uylings (1998). [c]*References*: (1) Barklem et al. (2000); (2) Barklem & Aspelund-Johansson (2005).

from the $2p^4$, $2p^3 3s$, $2p^3 3p$, $2p^3 3d$ multireference (MR) configurations to the {9s, 9p, 9d, 6f, 6g, 6h} orbital active set (where the maximum orbital principal quantum number n_{max} is specified for each orbital azimuthal quantum number $l = s$–h). The core-valence effects were included by means of single and double excitations from 1s to the active set of orbitals. The convergence of the oscillator strengths for the O I lines was verified by comparing the results obtained using physical models including increasingly large active sets of orbitals and by observing a good agreement between the gf-values computed within the Babushkin (B) and the Coulomb (C) gauges. The two gauges tend to preferentially weight different parts of the wavefunctions (that is the outer region vs. near-nucleus) and so, it can be used to quantify the systematic effects.

We also performed large, exhaustive calculations of f-values for the diagnostic lines of O I and N I using the code AUTOSTRUCTURE (Badnell 2011). We considered all one-, two-, and three-electron promotions from the 2s and 2p orbitals of configurations $2s^2 2p^4$ to excited orbitals nl, with $3 \leq n \leq 6$ and $0 \leq l \leq 4$. We analysed the convergence or lack thereof of the oscillator strengths with increasingly large configuration expansions, which accounted for hundreds of configurations for each element. In every calculation we made use of term energy corrections and level energy corrections, which are semi-empirical corrections available in AUTOSTRUCTURE. Convergence of calculated oscillator strength values was evaluated by two criteria that are the stability of the numeric values as more configurations are accounted for in the configuration interaction

expansion and the agreement between calculated length and velocity gauges of the oscillator strength.

The comparison of the f-values with the literature estimates is provided in Table 3. The values obtained with the MCDHF method and with AUTOSTRUCTURE agree to better than 1.5% for the velocity gauges, and 5% for the length gauges. Our results are also in a good agreement with the literature, including the values published by Hibbert et al. (1991) and by Jönsson & Godefroid (2000).

Our recommended values for the O I triplet lines are based on our new estimates calculated with both the MCDHF approach and AUTOSTRUCTURE. The final values of oscillator strengths are $\log gf = 0.350, 0.204$, and -0.019 dex for the 777.1, 777.4, and 777.5 nm transitions, respectively. These f-values are nearly identical to those adopted by Bergemann et al. (2021), with a difference of 1.6% only. The 630 nm line is an M1 transition and the transition operator is gauge independent. For this transition, our best value is the MCDHF result ($\log gf = -9.69$ dex), because it includes relativistic and electron correlation effects in more detail than the SST and HFR+CPOL calculations. The differences between different methods and between the two gauges are used to estimate the uncertainties of our f-values using the standard expression used in atomic physics $\mathrm{d}T = |gf(\mathrm{B}) - gf(\mathrm{C})|/\max(gf(\mathrm{B}), gf(\mathrm{C}))$. It is important to note that there is no reason to prefer one gauge over the other. The convergences of the f-values in both of them demonstrate a similar behaviour. We therefore advocate using the averages of results obtained in length and velocity form or their relativistic equivalents.

2.7. Line lists

We made use of the line list compiled for the *Gaia*-ESO survey (GES) that is described in Heiter et al. (2021). It includes basic atomic data (wavelengths, energy levels, transition probabilities, broadening constants) and quality flags for lines relevant to FGK stars in the wavelength range from 475 to 685 nm and from 849 to 895 nm. The line list was assembled by a dedicated GES working group after a detailed assessment of all available sources of atomic and molecular data, with priority given to experimental data and carefully validated theoretical data. For a subset of atomic transitions tabulated in the line list, a pair of flags is given for each transition that indicates the quality of the atomic data (primarily, $\log gf$) and the quality of the line in the stellar spectrum (primarily, blending). For each of these two aspects, the lines were sorted into three categories of decreasing quality, designated 'Y', 'U', and 'N'. The quality assessment was based on a comparison of synthetic and observed spectra for the Sun and Arcturus.

Since the GES line list only includes atomic data published until 2014, we updated the entries whenever more recent datasets have become available in the literature. The data and references for all the spectral lines used for the abundance calculations are given in Tables 1 and 2. For the diagnostic lines, van der Waals broadening parameters were adopted, where available, from Barklem et al. (2000). Also for the other lines in the linelist, we gave preference to the Anstee-Barklem-O'Mara theory (Anstee & O'Mara 1991 and successive expansions by P. S. Barklem and Collaborators). Tables 1 and 2 give the values in a packed notation where the integer component is the broadening cross-section, σ, in atomic units, and the decimal component is the dimensionless velocity parameter, α. Values less than zero are the logarithm of the broadening width per unit perturber number density at 10 000 K in units of rad s^{-1} cm^3.

The oscillator strengths were adopted from the following sources. For C I, we used the new f-values from Li et al. (2021), which were computed by means of multiconfiguration Dirac-Hartree-Fock and relativistic configuration interaction methods. We note that for most transitions, they are systematically lower compared to the commonly used values from Hibbert et al. (1993). For the Mg I lines at 5528 Å and 5711 Å, we used the experimental gf-values from Pehlivan Rhodin et al. (2017). For the Ca I line at 6455.598 Å, we updated the value in the GES line list to that recommended in Den Hartog et al. (2021). Also, the other Ca I lines that we used are included in the list of recommended lines by Den Hartog et al. (2021), and the uncertainties quoted in Table 1 are those recommended by Den Hartog et al. (2021)[6]. Most of the lines used for the abundance calculations that are also included in the GES line list have gf-value quality flag 'Y', except for a few Fe lines with flag 'U'. Concerning the blending quality flag, most lines have flag 'Y' or 'U', except for two Ni I lines (at 4811.983 and 4814.598 Å) with flag 'N'. However, these two lines are clearly blended only in the spectrum of Arcturus, and much less so in the spectrum of the Sun.

For the wavelength ranges not covered by the GES line list, we used data from the VALD database[7] (Piskunov et al. 1995; Ryabchikova et al. 2015), complemented with molecular line lists provided by B. Plez (priv. comm.). It should be noted, however, that special care was taken to select only lines minimally affected by blends. Therefore the inclusion of molecules in the spectrum synthesis is strictly speaking not necessary, except for the modelling of N I lines, which are blended by CN features.

3. Results

Our results for all relevant chemical elements are collected in Table 4, and in Table 5 we provide the abundances of all species that are relevant to the SSM. To illustrate the quality of the spectral fits, we show selected examples of the best-fit spectra compared to the observed profiles in Fig. 4. Abundances measured from individual lines are presented in Table A.1.

The uncertainties of the abundances were derived in analogy to Bergemann et al. (2021). We form uniform distributions of errors using the values representing (a) the uncertainty of the transition probability (f-value); (b) the systematic uncertainty caused by using different ⟨3D⟩ models; (c) the uncertainty caused by the H collisional data (only for elements treated in NLTE); and (d) the statistical uncertainty. The latter is represented by the scatter of abundances derived from individual spectral lines of the same chemical element (shown in the last column of Table 4). The uncertainty caused by using different ⟨3D⟩ models is represented by the difference between the abundances derived with ⟨3D⟩ STAGGER and CO5BOLD models (see the fourth column of Table 4). The error distributions were then co-added, as the uncertainties are independent. Since the shapes of the distributions are close to Gaussian, we adopt the simple averages and the standard deviations (1σ) of the resulting combined distributions as our final abundances and their corresponding uncertainties, respectively.

[6] These uncertainties refer to the absolute gf-values, while the uncertainties given in the GES line list are those of the relative measurements quoted in Smith & Raggett (1981) and Smith (1988).
[7] http://vald.astro.uu.se

Table 3. Comparison of log gf-values for the O I transitions.

Reference	Transition				
	777.1 nm	777.4 nm	777.5 nm	630.0 nm	$3s^5S^o–3p^5P$
Hibbert et al. (1991)					
CIV3 (L) [a]	0.371	0.225	0.003		0.702
CIV3 (V) [a]	0.333	0.187	−0.035		0.664
Jönsson & Godefroid (2000)					
MCHF (L) [b]					0.682
MCHF (V) [b]					0.679
Civiš et al. (2018)					
QDT [c]	0.317	0.170	−0.051		0.647
Storey & Zeippen (2000)					
SST [d]				−9.72	
This work					
HFR+CPOL [e]	0.350	0.204	−0.018	−9.65	0.681
MCDHF (B) [f]	0.370	0.224	0.002		0.701
MCDHF (C) [f]	0.331	0.184	−0.039		0.662
MCDHF [f]				−9.69	
AST (L) [g]	0.348	0.199	−0.021		
AST (V) [g]	0.326	0.176	−0.043		
Final recommended					
	0.350	0.204	−0.019	−9.69	

Notes. See text. [a]CIV3 calculations in the length (L) and velocity (V) gauges. [b]Non-relativistic multiconfiguration Hartree-Fock (MCHF) calculations in the length (L) and velocity (V) gauges. [c]Quantum Defect Theory (QDT). [d]SUPERSTRUCTURE (SST) calculations. [e]Pseudo-relativistic Hartree-Fock method including core-polarisation effects (HFR+CPOL). [f]Fully relativistic multiconfiguration Dirac-Hartree-Fock (MCDHF) calculations in the Babushkin (B) and Coulomb (C) gauges. [g]AUTOSTRUCTURE (AST) calculations in the length (L) and velocity (V) gauges.

Table 4. Solar photospheric abundances derived in NLTE.

El.	A(El), σ_{tot} 1D [a] NLTE	A(El), σ_{tot} ⟨3D⟩ [b] NLTE [c]	$\Delta_{STAGGER-CO5BOLD}$	σ_{stat}
C	8.48 ± 0.08	8.56 ± 0.06	0.016	0.05
N	7.88 ± 0.12	7.98 ± 0.10	−0.011	0.1
O	8.74 ± 0.04	8.77 ± 0.04	0.014	0.02
Mg	7.45 ± 0.08	7.55 ± 0.06	0.020	0.06
Si	7.54 ± 0.07	7.59 ± 0.07	0.005	0.06
Ca	6.34 ± 0.05	6.37 ± 0.05	0.026	0.04
Fe	7.49 ± 0.08	7.51 ± 0.06	0.012	0.08
Ni	6.21 ± 0.04	6.24 ± 0.04	0.001	0.07

Notes. See the text for details. [a]1D MARCS model atmosphere. [b]⟨3D⟩ STAGGER model atmosphere. [c]LTE for C and N.

3.1. New estimates of photospheric abundances

3.1.1. C

Our analysis of the C abundance relies on atomic C lines because these are the features we expect to be able to measure in the spectra of upcoming facilities, such as 4MOST and WEAVE. Since the diagnostic lines of C I are almost insensitive to NLTE (see below), we relied on ⟨3D⟩ LTE calculations to obtain the solar C abundance of A(C) = 8.56±0.06 dex. For comparison, the values obtained by Amarsi et al. (2019) and Caffau et al. (2010) are 8.44 ± 0.02 dex and 8.50 ± 0.06 dex, respectively, the latter in agreement with our work. Also, the revised 3D NLTE abundance by Li et al. (2021) is 8.50 ± 0.07 dex, which is consistent with our value. We note that using the new f-values calculated by Li et al. (2021), we obtain a significantly improved agreement between different C I lines, compared to the result obtained using the older f-values from Hibbert et al. (1993). The line-by-line scatter drops from 0.08 dex (with Hibbert et al. 1993 values) to 0.05 dex (with Li et al. 2021 values). In particular, the much lower log gf for the 7113.18 Å line found by the latter study is essential to bringing the line into agreement with the other optical lines of C I. This result suggests that the new f-values from Li et al. (2021) are more reliable than the older values from Hibbert et al. (1993).

Another estimate of the solar C abundance was recently presented by Alexeeva & Mashonkina (2015), who obtained (in 3D) A(C) = 8.43 ± 0.02 dex from the analysis of the CH lines, A(C) = 8.46 ± 0.02 dex from the C_2 lines, A(C) = 8.43 ± 0.03 dex from the C I permitted lines, and A(C) = 8.45 dex from the forbidden [C I] feature. However, these estimates rely on older Hibbert et al. (1993) data, and after re-normalisation to the

Table 5. Our recommended solar chemical abundances on the astronomical scale $A(i) = \log(N(i)/N_{\rm H}) + 12$.

Element	$A(El)_{ph}$, σ_{tot}	Ref.	$A(El)_{met}$, σ_{stat}
H	12.0	–	–
C	8.56 ± 0.05	1	–
N	7.98 ± 0.08	1	–
O	8.77 ± 0.04	1	–
F	4.40 ± 0.25	2	4.67 ± 0.09
Ne	8.15 ± 0.11	1	–
Na	6.29 ± 0.02	3	6.33 ± 0.04
Mg	7.55 ± 0.05	1	7.58 ± 0.02
Al	6.43 ± 0.03	4	6.48 ± 0.03
Si	7.59 ± 0.07	1	7.57 ± 0.02
P	5.41 ± 0.03	5	5.48 ± 0.03
S	7.16 ± 0.11	6	7.21 ± 0.03
Cl	[5.25 ± 0.12]	7	5.29 ± 0.07
Ar	[6.50 ± 0.10]	7	–
K	5.14 ± 0.10	3	5.12 ± 0.02
Ca	6.37 ± 0.04	1	6.32 ± 0.03
Sc	3.07 ± 0.04	3	3.09 ± 0.03
Ti	4.94 ± 0.05	8	4.96 ± 0.03
V	3.89 ± 0.08	9	4.01 ± 0.03
Cr	5.74 ± 0.05	10	5.69 ± 0.02
Mn	5.52 ± 0.04	11	5.53 ± 0.03
Fe	7.50 ± 0.06	1	7.51 ± 0.02
Co	4.95 ± 0.04	12	4.92 ± 0.02
Ni	6.24 ± 0.04	1	6.25 ± 0.03
Z/X	0.0225 ± 0.0014		0.0226 ± 0.0014 ± 0.0003

Notes. Uncertainties listed for the meteoritic abundances are purely statistical but a systematic and fully correlated 0.02 dex uncertainty should be included for all elements (Sect. 3.3). The last row reports the total Z/X, where the abundances of volatile elements are always taken from the photospheric scale. For the meteoritic scale, the second uncertainty source reflects the fully correlated uncertainty from transforming the cosmochemical scale to the astronomical scale. See the text for details.
References. (1) This work; (2) Maiorca et al. (2014); (3) Zhao et al. (2016); (4) Nordlander & Lind (2017); (5) Scott et al. (2015a); (6) Caffau et al. (2011); (7) Lodders (2019); (8) Bergemann (2011); (9) Scott et al. (2015b); (10) Bergemann & Cescutti (2010); (11) Bergemann et al. (2019); (12) Bergemann et al. (2010).

Li et al. (2021) f-values[8] their abundance is in excellent agreement with our result. Our analysis of C abundances is carried out in LTE, however, according to 3D NLTE calculations by Amarsi et al. (2019, their Table 2), 3D NLTE and 3D LTE abundances based on our diagnostic lines of C I agree within 0.01 dex.

Our estimate of the C abundance obtained using the CO5BOLD model is less than 0.02 dex lower compared to that calculated using the STAGGER model. This suggests that the difference between Caffau et al. (2010) and Amarsi et al. (2019) is likely not caused by the differences between the two 3D solar model atmospheres. The value provided by Asplund et al. (2021) is A(C) = 8.46 ± 0.04 dex, somewhat higher compared to the previous estimate by Asplund et al. (2009).

[8] The values from Li et al. (2021) are typically 0.05 dex to 0.16 dex lower for the diagnostic optical lines of C I. Hence, the C abundance is correspondingly higher.

3.1.2. N

Our estimate of the N abundance relies on the modelling of the two least-blended N I lines in the solar spectrum. For the lack of an NLTE model of N, we resort to the LTE analysis. The recent study by Amarsi et al. (2020) suggests that the difference between 1D LTE and ⟨3D⟩ NLTE abundances for the optical N I lines are extremely small, not exceeding 0.005 dex. In this work, we employ the new f-values calculated as described in Sect. 2.6. Our recommended value of the solar N abundance thus becomes A(N) = 7.98 ± 0.10 dex. The study by Amarsi et al. (2020) advocated for the solar N abundance of A(N) = 7.77 ± 0.05 dex, while Asplund et al. (2021) derived N abundance based on both atomic and molecular lines, A(N) = 7.83 ± 0.07, with a value unchanged from that of Asplund et al. (2009), where A(N) = 7.83 ± 0.05 dex. We note, however, that the N abundance has a very minor impact on the overall metallicity (see Sect. 3.4 and Fig. 7).

In the choice of the solar N value, it is important to stress that in this work we rely on ab-initio atomic and molecular data, and we do not apply any empirical adjustment to the line lists. In particular, all molecular features are included self-consistently in the radiative transfer and spectrum synthesis calculations. In contrast, the solar N abundance provided by Amarsi et al. (2020) is based on re-scaling the strengths of the CN blends in a semi-empirical approach, by estimating their equivalent widths in the solar disc-center spectrum through a comparison with nearby CN lines. While both approaches have their pros and cons, the main value of our strictly theoretical approach is that it is universal and can be applied to any star, without biasing the result by the assumed value of the observed disc-center equivalent widths of the CN blends. We find that abundance obtained using the CO5BOLD model is only 0.011 dex higher compared to that calculated using the STAGGER model.

3.1.3. O

Our result for O, namely: A(O) = 8.77 ± 0.04 dex, is in excellent agreement with the full 3D NLTE analysis by Bergemann et al. (2021, 8.75 ± 0.03 dex). The difference between the two results, which is not significant, is caused by using the flux spectrum and the average ⟨3D⟩ atmosphere model in this work.

Our O abundance is also consistent with the value by Caffau et al. (2008, 8.76 ± 0.07 dex), but it is somewhat higher compared to the estimate by Asplund et al. (2021, 8.69 ± 0.04 dex) and Amarsi et al. (2021, 8.70 ± 0.04 dex). These differences can be attributed to the use of new $\log gf$ values for the O lines, new observational material, and our first self-consistent NLTE radiative transfer for both O and Ni features, which is important for the critical diagnostic [O I] feature at 630 nm. As investigated in Bergemann et al. (2021) in detail, quantitatively, the break-down of systematic difference with Asplund et al. (2021) is as follows. Our new f-values lead to +0.02 dex higher abundances for the 777 nm lines, but −0.03 dex lower values for the 630 nm [O I] line. The IAG data further lead to a +∼0.02 higher abundance for the 777 nm and +0.03 dex higher values compared to the SST data, the SST data are however affected by the problem of fringing (Sect. 4.4 in Bergemann et al. 2021). Modelling Ni in NLTE leads to a ∼0.03 dex higher O abundance inferred from the [O+Ni] feature at 630 nm. There are also very minor differences caused by the continuum placement, model atmospheres, and resolution in radiative transfer modelling. Our results (Table A.1) for the 630 nm and 777 nm lines are in excellent agreement.

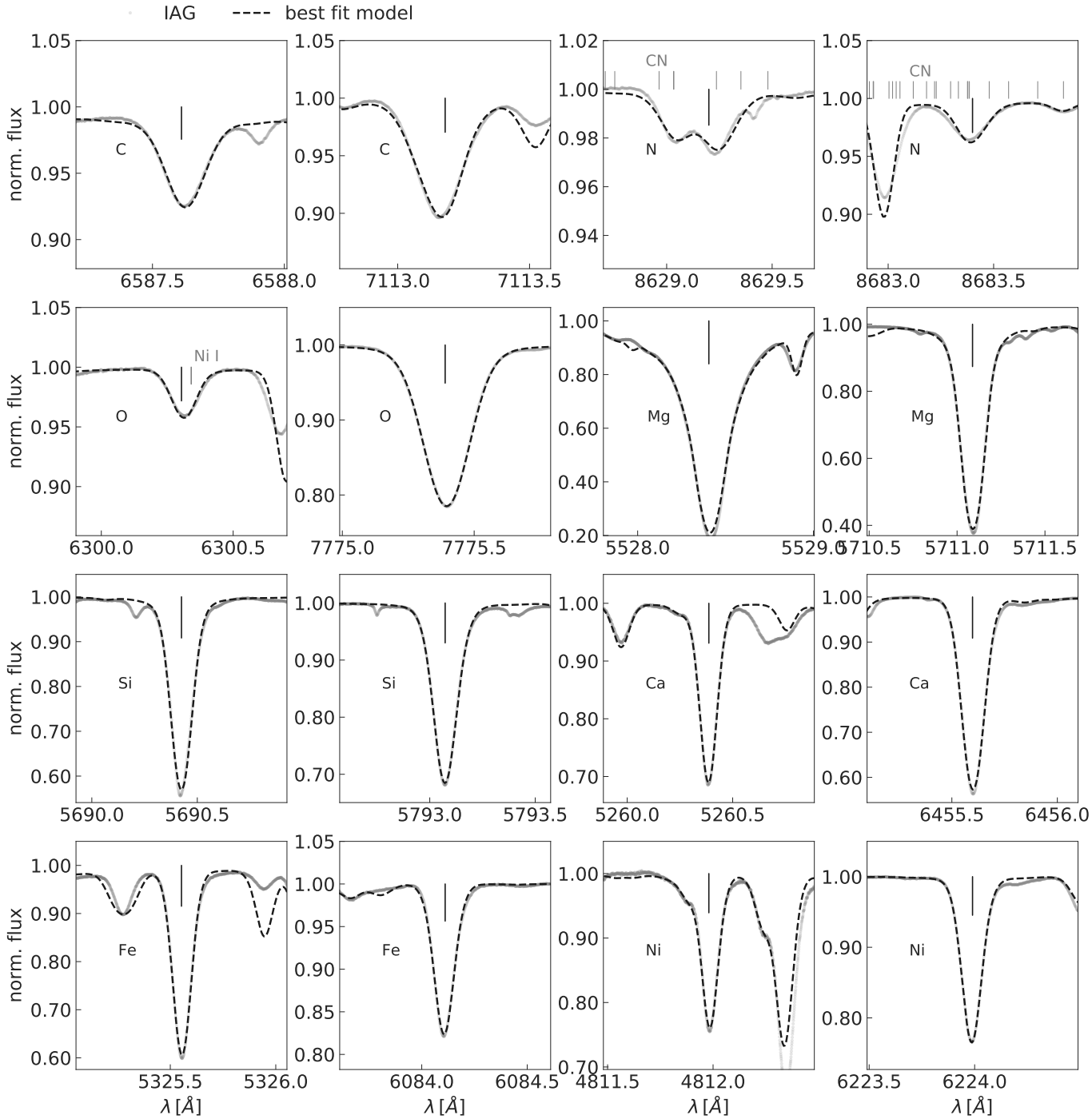

Fig. 4. Comparison of model and observed line profiles for some of the diagnostic lines.

Overall, our new O abundance is closer to the classical values from Grevesse & Sauval (1998) than the previous estimate by Asplund et al. (2021). We also note that according to Caffau et al. (2013), there is still an unresolved mismatch between the 630 nm and 636 nm [O I] lines, with the latter line yielding an the O abundance of 8.78 ± 0.02 dex.

To estimate the difference between the STAGGER and CO5BOLD models, we then performed a comparative analysis of the results obtained with both simulations. We find that the CO5BOLD model leads to a 0.006 dex lower abundance for the 630 nm forbidden line, and to 0.015 dex lower abundance for the permitted 777 nm O I triplet. This difference is not significant enough to explain the differences between the Caffau et al. (2008) and Asplund et al. (2009) results.

3.1.4. Mg

Our estimate of the solar photospheric abundance of Mg is A(Mg) = 7.55 ± 0.06 dex. Compared with the value obtained by Bergemann et al. (2017), 7.56 ± 0.05 dex, we find a very good agreement. Our results also support the recent detailed analysis of Mg in NLTE by Alexeeva et al. (2018), who found a value of A(Mg) = 7.54 ± 0.11 dex based on Mg I and A(Mg) = 7.59 ± 0.05 dex based on Mg II lines. The comparison of abundances obtained from the CO5BOLD and STAGGER ⟨3D⟩ models

(Table 4) suggests that the atomic Mg lines used in this work (at 5528 and 5711 Å) are not sensitive to the differences between the ⟨3D⟩ model atmospheres, with the difference in abundance not exceeding 0.02 dex.

The main uncertainty in the analysis of Mg abundances is still associated with the errors of the oscillator strengths and damping parameters. For comparison, the ⟨3D⟩ NLTE solar Mg abundance from Osorio et al. (2015) is considerably higher, 7.66 ± 0.07 dex. The offset could possibly be explained by the differences in the model atom, adopted atomic data, and the choice of lines in the calculations. Osorio et al. (2015) find significant (+0.05 to +0.15 dex) differences between the Mg abundances derived from the Mg I lines using the 1D and ⟨3D⟩ solar model atmospheres. This is confirmed by our analysis.

3.1.5. Si

The Si abundance is a very important parameter in the analysis, as the element has traditionally been used as the main anchor between the solar photospheric and the meteoritic abundance scales (Lodders 2003, 2019; Asplund et al. 2009). Our ⟨3D⟩ NLTE value, A(Si) = 7.59 ± 0.07 dex is slightly higher compared to the recent 3D NLTE estimate by Amarsi & Asplund (2017) and more recently by Asplund et al. (2021).

For the Si I lines, the NLTE effects are negative, such that NLTE abundances are lower compared to LTE values (Shi et al. 2008; Bergemann et al. 2013; Mashonkina 2020), which is also supported by our new results. Our NLTE abundances for all lines in the list are ∼0.03 to 0.05 dex lower compared to LTE. The most recent NLTE estimate of the solar Si abundance, based on the NLTE line-by-line spectrum synthesis, was presented in Mashonkina (2020). They found that NLTE abundances obtained from the solar Si I lines are on average 0.02 to 0.1 dex lower compared to LTE (their Table 2), fully in agreement with our findings. Using their results for the lines in common with our study and re-normalising them to employed in this study f-values, their A(Si) becomes 7.55 dex, fully in agreement with our 1D NLTE estimate. In fact, their solar Si abundance using their preferred f-values would be 7.60 dex for the lines in common between our and their study, thus about 0.1 dex higher compared to Asplund et al. (2021).

Si I lines are similar to Mg I in that the lines are barely affected by the detailed structure of the 3D model atmosphere. The difference between the results based on CO5BOLD and STAGGER does not exceed 0.005 dex.

3.1.6. Ca

The solar photospheric abundance of Ca is robust, as our ⟨3D⟩ NLTE calculations show an excellent consistency between different diagnostic lines of Ca I. Our recommended value is A(Ca) = 6.37 ± 0.05 dex. This value is slightly higher compared to the recommended value from Asplund et al. (2021, 6.30 ± 0.03 dex).

Other recent estimates of the solar Ca abundances were presented by Mashonkina et al. (2017) and Osorio et al. (2019). Mashonkina et al. (2017), performed a 1D NLTE analysis with the solar MARCS model, which resulted in solar abundances of A(Ca) = 6.33 ± 0.06 dex based on Ca I lines and A(Ca) = 6.40 ± 0.05 dex based on Ca II lines with high values of $E_{\rm low}$. The average of these quantities is consistent with our ⟨3D⟩ NLTE estimate, which is not surprising as their NLTE model atom and the chosen line list are similar to our inputs.

Osorio et al. (2019) also used 1D hydrostatic models in combination with NLTE line formation. However, their solar abundances show a significant scatter, ranging from A(Ca) = 6.0 dex to 6.45 dex, which likely results from the choice of lines in their analysis.

3.1.7. Fe

Our results for the solar Fe abundance are close the recent literature estimates. In ⟨3D⟩ NLTE, we obtained A(Fe) = 7.51 ± 0.06 dex, which represents the combination of the abundance determined from the Fe I and Fe II lines. The abundances derived from the lines of the neutral species are sensitive to NLTE, which is also known from literature studies (e.g. Bergemann et al. 2012; Lind et al. 2012). However, the majority of diagnostic lines in our line list have $E_{\rm low} \gtrsim 2.5$ eV, therefore the difference with the LTE abundance is not large and does not exceed 0.1 dex for the majority of Fe I lines. We do not include Fe I lines with low $E_{\rm low}$ values in the abundance analysis, due to their high sensitivity to the choice of model atmosphere, see Sect. 2.3. However, this choice of Fe lines affects the final Fe abundance by no more than 0.01 dex. Likewise, the abundance differences obtained from the CO5BOLD and STAGGER models do not exceed 0.012 dex.

Comparing our results with the recent estimates by two different groups, namely, Lind et al. (2017, 7.48 ± 0.04 dex) and Mashonkina et al. (2019, 7.54 dex), we find a good agreement with both studies. The latter estimate is based on the analysis of Fe II lines using the solar MARCS model atmosphere and the f-values from Raassen & Uylings (1998), whereas the former relies on 3D NLTE modelling of the lines of both ionisation species. Also, the careful systematic analysis of Fe lines in NLTE by Sitnova et al. (2015) supports our result, although these authors relied on the Drawin formula to describe Fe+H collisions instead of quantum-mechanical data.

Our solar Fe abundance is also fully consistent with the earlier estimate by Caffau et al. (2007), who found A(Fe) = 7.52 ± 0.06 dex, they also suggest that the result is not sensitive to the choice of f-values. The value from Asplund et al. (2021, 7.46 ± 0.04 dex) is, in contrast, significantly lower compared to our values, to Caffau et al. (2007), and to Mashonkina et al. (2019).

3.1.8. Ni

This work presents the first detailed analysis of the solar photospheric abundance of Ni using ⟨3D⟩ NLTE calculations. Our best estimate is A(Ni) = 6.24 ± 0.04 dex, based on the detailed modelling of 11 lines of Ni I and one line of Ni II using the f-values from Wood et al. (2014).

We did not detect any systematic trend with the excitation potential of the lower energy level or other atomic parameters, which bolsters our confidence in the results. The NLTE effects in the diagnostic solar Ni lines are modest: for the Sun, the differences between 1D NLTE and 1D LTE results are of the order 0.01 dex. However, as shown in Scott et al. (2015b) and in Bergemann et al. (2021), the lines of Ni are sensitive to the temperature structure of the model, and the calculations with models based on 3D RHD simulations yield somewhat higher Ni abundance in LTE and NLTE.

We also find that Ni lines are not very sensitive to the structure of the ⟨3D⟩ model atmospheres. The abundances derived with STAGGER model are within 0.02 dex different from the abundances derived using temporarily spaced CO5BOLD

snapshots. However, these differences average out when combining the results from individual CO5BOLD snapshots. Therefore, the final difference between STAGGER and CO5BOLD is negligible, namely, below 0.001 dex.

3.2. Other chemical elements

3.2.1. Ne, Cl, and Ar

The analysis of the Ne abundance is beyond the scope of this paper because the abundance of the element cannot be determined from the solar photospheric spectrum. It is common (e.g. Lodders 2019) to determine the solar Ne abundance from the Ne/O ratio that can be established independently and by assuming the ratio is the same in the solar photosphere, the absolute Ne abundance is derived.

This procedure was previously adopted by Lodders (2003), for instance, to derive the Ne abundance by combining the Ne/O ratio measured in young B type stars and He II regions (Meyer 1989), in solar active regions (Widing 1997), and in solar energetic particle events (Reames 1998) with the photospheric O abundances. Using the Ne/O ratio from Lodders (2003) (Ne/O = 0.152), and adopting our O abundance, we would obtain A(Ne) = 7.95 ± 0.1 dex. This value is consistent with that by Bochsler (2007), who obtained the Ne abundance by combining the solar wind data from the APOLLO foil experiment (Geiss et al. 1972), based on a model for the Coulomb-drag fractionation in the solar wind. Juett et al. (2006) determined the Ne/O ratio in the interstellar medium (ISM, 0.185) from the K- and L-shell spectroscopy of nine X-ray binaries. Whether the solar values and the ISM values are consistent is still debated, as the latter is, in particular, prone to systematic effects, such as the choice of the model describing the ionisation structure of the Local Bubble (e.g. Breitschwerdt & de Avillez 2021). The recent analysis of the local ISM data acquired with the IBEX satellite by Park et al. (2014) indicates a significantly higher Ne/O value of 0.33. This estimate supports the earlier values based on ISM data collected with the SWICS spectrometer on Ulysses (Ne/O = 0.26 dex, Gloeckler & Fisk 2007; their Table 3, estimated based on total densities of Ne and O in the local interstellar cloud). It is also consistent with the estimate based on the analysis of *Chandra* X-ray spectra (Ne X, O VIII, O VII) of nearby FGK-type main-sequence stars by Drake & Testa (2005, 0.41). Furthermore, a recent NLTE analysis of 24 B-type stars by Alexeeva et al. (2020) finds non-negligible differences with Ne abundances presented in Meyer (1989).

In the most recent analysis of the SOHO data with new atomic data, Young (2018) found a Ne/O ratio of 0.24 ± 0.05 dex. Using their value, we obtain A(Ne) = 8.15 dex, which is higher than the estimate calculated using the Ne/O fraction from Lodders (2003). In the light of remaining uncertainties associated with the ISM and B-type diagnostics, we have opted to determine our final Ne abundance using the Young (2018) Ne/O ratio, which is based on the SOHO measurements of emission lines from the transition region of the quiet Sun. That value is about 40% higher compared to an earlier estimate by the same author (Young 2005) because of the use of more accurate ionisation and recombination rate coefficients. We adopt a more conservative error to reflect the uncertainty associated with the latter, as well as the uncertainty of our photospheric O abundance. Our recommended abundance is, thus, A(Ne) = 8.15 ± 0.11 dex. The value is consistent with the estimate by Young (2018), A(Ne) = 8.08 ± 0.09 dex and 8.15 ± 0.10 dex, employing the O values from Asplund et al. (2021) and Caffau et al. (2011), respectively.

For Cl and Ar, we adopted the values from Lodders (2019). These elements do not play any significant role in the calculation of the SSM, however, we have included them here for completeness.

3.2.2. F, Na, K, P, Al, and S

We did not redetermine the abundance of these elements in this work. Rather, we relied on recent literature values, giving preference to the values that are most consistent with our methodological approach.

The solar abundance of F is taken from the analysis by Maiorca et al. (2014). To the best of our knowledge, no NLTE analysis of F has been performed to date. For both Na and K, we adopt the estimates from Zhao et al. (2016). They determined the Na abundance in NLTE using six Na I lines and the model atom from Gehren et al. (2004). The error of the Na value adopted for this study was calculated from the line-to-line scatter (presented in Table 2 in Zhao et al. 2016). The study by Scott et al. (2015a) advocates a solar Na abundance of 6.21 ± 0.04 dex.

The abundance of K determined by Zhao et al. (2016) and adopted for this study was based on the NLTE model presented in Zhang et al. (2006). Another NLTE estimate of the solar K abundance by Reggiani et al. (2019), A(K) = 5.11 dex, is fully consistent with that of Zhao et al. (2016).We adopt a conservative uncertainty of A(K) to be 0.1 dex, as neither Zhao et al. (2016) nor Reggiani et al. (2019) provide an uncertainty on their K abundance estimate. The abundance of P was taken from Scott et al. (2015a) and it is based on LTE, for the lack of NLTE calculations. The value of the Al abundance is taken from the 3D NLTE analysis by Nordlander & Lind (2017).

For S, we adopted the value from Caffau et al. (2007), A(S) = 7.16 ± 0.11 dex. Their estimate is based on the detailed analysis of several S I lines in the optical and near-IR solar spectrum using the CO5BOLD model atmosphere using NLTE abundance corrections from Takeda et al. (2005). Also, the NLTE analyses by Korotin (2009) and Korotin et al. (2017) suggest significant deviations from LTE for the majority of S I lines. Another recent estimate of the solar photospheric S abundance was proposed by Asplund et al. (2021), and it is slightly lower (A(S) = 7.12 ± 0.03 dex) compared to our adopted value.

3.2.3. Fe-peak elements

For Sc, we refer to the estimate provided by Zhao et al. (2016) using a set of Sc II lines modelled in NLTE with full account for hyperfine splitting (HFS). This estimate is preferred over other values, which were carried out in LTE (e.g. Lawler et al. 2019; Asplund et al. 2021). It should be noted that both Sc I and Sc II show significant departures from LTE, thus, the Sc II-based abundances are typically overestimated overall (Zhao et al. 2016). Our Sc value is in excellent agreement with the meteoritic abundance.

The solar abundances of Ti, Cr, and Co were adopted from Bergemann (2011), Bergemann & Cescutti (2010), and Bergemann et al. (2010), respectively. All these estimates are based on detailed NLTE modelling, with account for HFS for Co lines and isotopic shifts for Ti. Our value for the Mn abundance (A(Mn) = 5.52 ± 0.04 dex) was taken from the detailed analysis in Bergemann et al. (2019). This estimate is based on full 3D NLTE radiative transfer calculations of 13 Mn I lines, using the same 3D STAGGER model atmosphere as employed in this work. Bergemann et al. (2019) showed that taking into account

3D NLTE effects is essential to obtain reliable excitation-ionisation balance for Mn in atmospheric conditions of late-type stars.

3.3. Meteoritic abundance scale

CI-chondrites are a well known source to measure primitive solar system abundances of refractory elements (Lodders 2003, 2021). Meteoritic measurements have been historically more robust than photospheric determinations and the level of agreement between meteoritic and photospheric abundances has been used as a gauge of the quality of the latter. Bringing the meteoritic abundances to the photospheric scale requires defining an anchor point. The Si abundance has often been used for this purpose (Grevesse & Sauval 1998; Lodders 2003; Asplund et al. 2021), but groups of elements have been applied in such instances as well (Anders & Grevesse 1989; Palme et al. 2014).

Regardless of the methodology, meteoritic abundances converted to the photospheric scale have two uncertainty terms. The first one is the intrinsic error associated with the process of the abundance measurement that can be assumed uncorrelated among different elements. The second one is the systematic error associated with the transformation and it is a fully correlated error among all chemical elements. As a result, these two error sources cannot be quadratically added. This error source when meteoritic abundances are used for calculation of solar (stellar) models has been traditionally ignored and, unfortunately, can be equal or even larger than the measurement error. Our goal below is to obtain meteoritic solar abundances for which the systematic component of the error is minimised, that is, the anchor point is defined more robustly.

To this end, we adopted the CI-chondrite abundances from Lodders (2021) in the cosmochemical scale, defined such that the Si abundance is $N(\mathrm{Si}) = 10^6$. In order to derive meteoritic abundances in the astronomical scale, we introduced a scale factor, c. We determine the latter by minimising the quadratic difference between the photospheric and meteoritic scales using the set of five refractory elements that have been newly derived in this work, constructed as

$$\chi^2 = \sum_i \frac{\left[A(i)_{\mathrm{ph}} - (\log N_i + c)\right]^2}{\sigma^2_{i,\mathrm{ph}} + \sigma^2_{i,\mathrm{me}}}, \quad (1)$$

where the sum extends over Mg, Si, Ca, Fe, and Ni. We obtained an excellent agreement between the two scales, yielding a total $\chi^2_{\mathrm{min}} = 1.27$, for $c = 1.57 \pm 0.02$[9]. The uncertainty in c is determined by the range over which $\Delta\chi^2 = 1$ around the minimum. It represents the systematic uncertainty associated to the meteoritic scale that should be included for all elements and it is also a fully correlated error source among them. For comparison, Lodders (2003) obtained $c = 1.54$ using only Si, but did not include an estimate of the systematic error. The final meteoritic abundances transformed to the solar photospheric abundance scale and the associated measurement errors are listed in Table 5. The systematic and fully correlated 0.02 dex error is not included in the table but should always be taken into consideration when assessing the uncertainties due to chemical composition uncertainties in solar and stellar models.

Our final estimate of the solar Z/X ratio is 0.0225, if calculated using the photospheric abundances only, and 0.0226, if the meteoritic abundances are used for most species – except C, N, and O, for which the photospheric values are used. Our Z/X ratio is 26% higher compared to Asplund et al. (2009), Z/X = 0.0181. It very close (within 1%) to the photospheric and meteoritic estimates by Grevesse & Sauval (1998), Z/X = 0.0231 and 0.0229 respectively, although the internal distribution of metals is different. And it is almost 10% higher than the estimate by Caffau et al. (2011), Z/X = 0.0209.

[9] Before rounding, the result is $c = 1.567 \pm 0.023$.

3.4. Standard solar models

The choice of the solar chemical mixture has a direct impact on SSMs because they are calibrated to reproduce the adopted photospheric chemical mixture at the present-day solar age. In this way, the abundance of metals in the interior of SSMs is determined by the photospheric abundances. Metals are main contributors to the radiative opacity in the solar interior which, in turn, determines the mechanical and thermal structure of the model.

A broadly used diagnostic for the quality of SSMs is the comparison of the sound speed profile of the model against the solar profile as inferred from helioseismic techniques. The deficiency of SSMs calibrated on solar mixtures based on results from Asplund (2005), and Asplund et al. (2009), along with the much better results for SSMs based on the solar mixtures by Grevesse & Noels (1993), Grevesse & Sauval (1998), are well documented (Bahcall et al. 2005; Basu & Antia 2008; Serenelli et al. 2009; Pinsonneault & Delahaye 2009; Serenelli et al. 2011; Buldgen et al. 2019). The solar mixture by Caffau et al. (2011) slightly improves the comparison, owing to overall higher (10 to 30%, depending on the element) abundances of CNO with respect to Asplund et al. (2009) and, to a minor extent larger abundances of refractories.

Here, we compute new SSMs using the GARSTEC code (Weiss & Schlattl 2008), based on the photospheric and meteoritic solar mixtures provided in Table 5 (MB22-phot and MB22-met models, respectively). The physics included in the models is the same as in Vinyoles et al. (2017). Atomic opacities have been computed for both flavors of MB22 solar mixtures, using OPCD 3.3 routines (Badnell et al. 2005). Opacities at low temperatures are most sensitive to the chemical composition, thus we computed those using the revised MB22 mixture as described in Ferguson et al. (2005).

New helioseismic inversions of the solar sound speed were performed for all the SSMs used in this work, based on the methodology described in Basu et al. (2009), and references therein, using the helioseismic data described in Basu (2021). The fractional sound speed differences are shown in Fig. 6. For comparison, we overplot the new inversion results for the SSMs computed with the Asplund et al. (2021, AAG21), Caffau et al. (2011, C11), Asplund et al. (2009, AGSS09-met), and Grevesse & Sauval (1998, GS98) compositions. The figure also includes (shaded area) the uncertainty in the sound speed profile due to uncertainties in the SSM inputs computed using the method from Villante et al. (2014) (see also below).

Results show that SSMs based on the solar mixtures obtained in this work reproduce the solar sound speed profile with much greater accuracy than the AGSS09-met model and, interestingly, at a comparable level to the GS98 SSM. This is due to the higher metal abundances found in this work, in particular for O, and to a lesser extent refractories, compared to the results of Asplund et al. (2009). The similarity between results of the MB22 SSMs and GS98 could be expected given that the global $(\mathrm{Z/X})_\odot$ is very similar. However, it is important to highlight that the internal distribution of elements is different in our and GS98 solar mixtures and the agreement in Z/X is a numerical coincidence. For instance, for two critical elements, O and Si, our

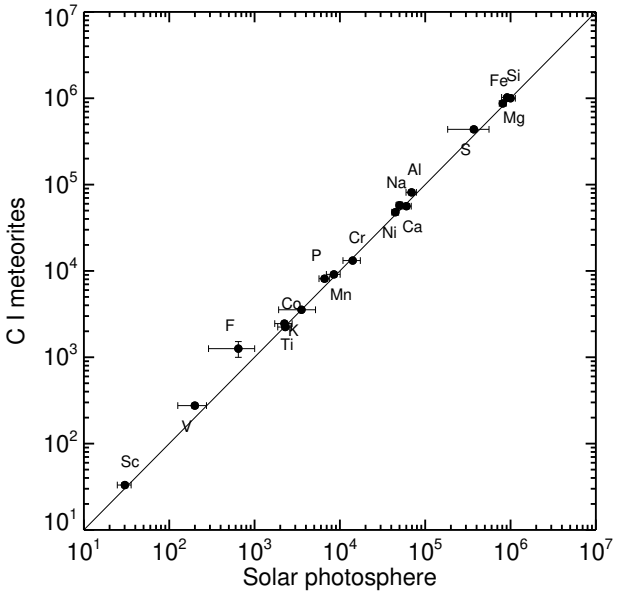

Fig. 5. Comparison of the photospheric estimates with meteoritic values.

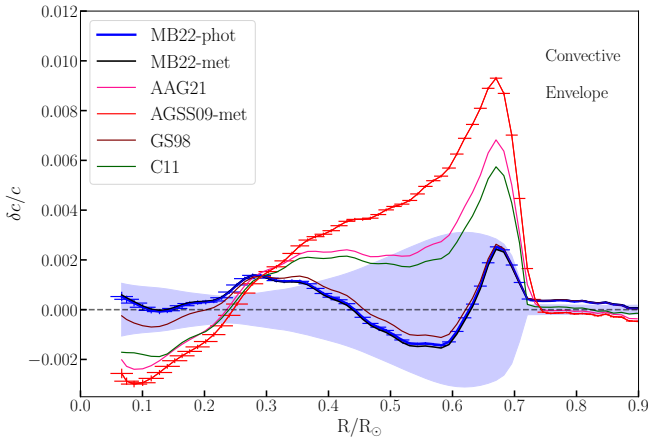

Fig. 6. Sound speed profiles of the SSM computed using different solar chemical mixtures, Caffau et al. (2011, C11), Asplund et al. (2009, AGSS09-met), Grevesse & Sauval (1998, GS98), Asplund et al. (2021, AAG21), and this work (MB22-phot and MB22-met, see Sect. 3.3 for details). The shaded blue area represents the solar model uncertainties arising from the inputs to the model, see Villante et al. (2014) for details. Error bars in AGSS09-met and MB22-phot lines denote fractional sound speed uncertainties arising from helioseismic data (y-axis) and the widths of inversion kernels (x-axis).

values are 15% lower and 10% higher, respectively, compared to GS98. For completeness, we have included a SSM based on the Asplund et al. (2021) composition which shows a partial improvement with respect to the AGSS09-met model, but still far from the SSMs based on the solar mixtures determined in the present work.

To quantify the impact of solar abundances on the sound speed profile, we follow Villante et al. (2014) and we show the logarithmic partial derivatives of the sound speed profile with respect to the abundance of individual elements in the left panel of Fig. 7. These derivatives depend only slightly on the reference solar mixture but some differences with respect to Villante et al. (2014) can be observed. The right panel of Fig. 7 shows the actual fractional sound speed uncertainty in the models due to uncertainties is solar abundances, with chemical elements grouped as indicated in the figure and using the photospheric uncertainties given in Table 5. The uncertainty in Ne plays a dominant role in the regions below the convective envelope. The uncertainty due to refractory elements is dominant below $0.45\,R_\odot$. This is different from previous results on SSMs (see e.g. Vinyoles et al. 2017) and is due to the larger spectroscopic uncertainties given in the present work.

A summary of relevant characteristics of SSMs used in this work is given in Table 6. The depth of the convective envelope, R_{CZ}, and the surface helium abundance Y_S are two widely used helioseismic probes of SSMs and should be compared to their observational values: $0.713 \pm 0.001\,R_\odot$ (Basu & Antia 1997) and 0.2485 ± 0.0034 (Basu et al. 2004), respectively. We note that despite the fact that our photospheric Z/X is almost equal to that of GS98, the value of Z_{ini} in the MB22 models is 5% lower than in the GS98 SSM. This is due to the higher abundance of refractories in our results, which results in a slightly higher opacity in the solar core and a higher Y_{ini} (or lower initial hydrogen) to satisfy the solar luminosity constraint. In addition, we provide the averaged rms of the sound speed fractional difference. While it is beyond the scope of this paper to present a complete analysis of the comparison between SSMs and helioseismic observations, it is clear that our newly derived solar mixture improves the agreement between the observed helioseismic characteristics of the Sun and SSMs. Our results are close to those based on GS98 solar mixture, despite the drastically different approaches. As shown in Fig. 5, the agreement between the photospheric and meteoritic scales is excellent. This is also reflected by the similarity of the results obtained with the MB22-photo and MB22-met SSMs.

The SSM presented in the current work provides a good consistency with the solar structure based on helioseismic observations. While SSMs offer an incomplete description of the physics in the solar interior, current results alleviate the need for more complex physics, such as accretion of metal-poor material (Serenelli et al. 2011), energy transport by dark matter particles (Vincent et al. 2015), revision of opacities (Bailey et al. 2015), enhanced gravitational settling, and other effects (Guzik & Mussack 2010).

4. Conclusions

In this work, we used new observational material for the Sun, new updated atomic data, and up-to-date NLTE model atoms to re-analyse the detailed chemical composition of the solar photosphere. For O I, we re-computed the oscillator strengths using several independent approaches, finding excellent agreement between the new values and those adopted in Bergemann et al. (2021). New $\log(gf)$ values were also computed for N I transitions. We used two families of 3D radiation-hydrodynamics simulations of solar convection, CO5BOLD and STAGGER, to represent the solar atmosphere, which allowed us, for the first time, to quantify the differences between the abundances inferred with both models. We focused on carrying out the analysis in such a way that it can be applied directly to stars observed within ongoing and upcoming large-scale spectroscopic surveys, such as 4MOST, WEAVE, and SDSS-V.

We provided new estimates of chemical abundances for elements most relevant for the calculations of standard solar models, including C, N, O, Mg, Si, Ca, Fe, and Ni. We complement these results with estimates of the solar abundances of Mn, Ti, Co, Cr, and Sr from our previous studies based on NLTE. Comparing our abundances of refractories with the element ratios

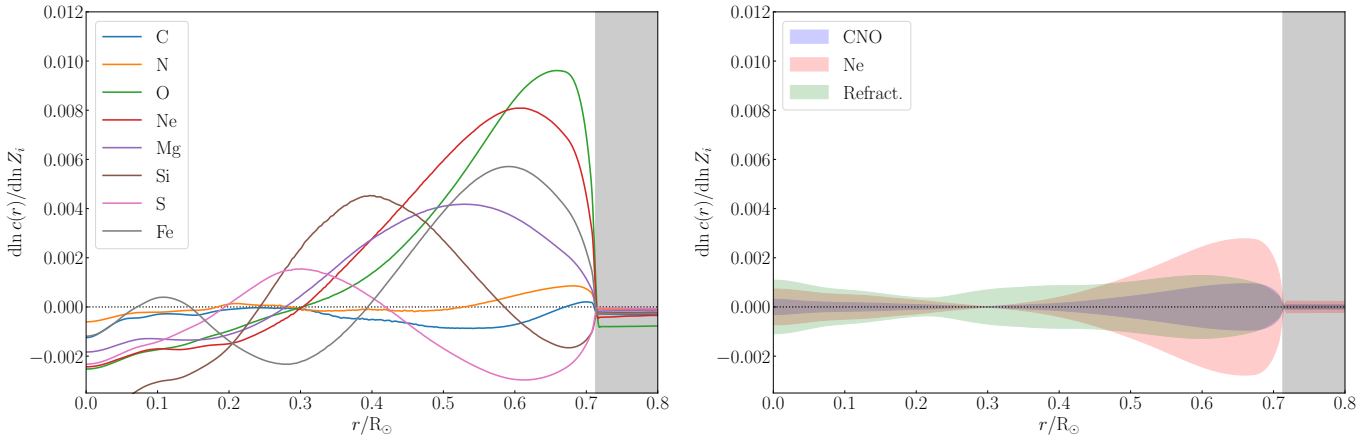

Fig. 7. Impact of solar abundances on the reference solar mixture. *Left panel*: logarithmic partial derivatives of the sound speed with respect to element abundances. *Right panel*: fractional 1σ uncertainties in the solar model sound speed based on photospheric abundances for different groups of elements, as indicated.

Table 6. Main characteristics of SSMs used in this work.

Model	$R_{\mathrm{CZ}}/R_\odot$	Y_{S}	$\langle\delta c/c\rangle$	Y_{ini}	Z_{ini}
MB22-phot	0.7123	0.2439	0.0010	0.2734	0.0176
MB22-met	0.7120	0.2442	0.0010	0.2737	0.0178
AAG21	0.7197	0.2343	0.0027	0.2638	0.0155
AGSS09-met	0.7231	0.2316	0.0041	0.2614	0.0149
GS98	0.7122	0.2425	0.0010	0.2718	0.0187
C11	0.7162	0.2366	0.0021	0.2658	0.0169

Notes. Columns are depth of convective envelope R_{CZ}, surface helium mass fraction Y_{S}, fractional sound speed rms, $\langle\delta c/c\rangle$, and initial helium, Y_{ini}, and metal, Z_{ini}, mass fractions.

based on CI chondrites, we find an excellent agreement between the two scales. We find that for most species, our abundances are in good agreement with other literature values obtained with detailed NLTE methods for 1D and 3D model atmospheres (e.g. Caffau et al. 2011; Osorio et al. 2015; Alexeeva et al. 2018; Mashonkina et al. 2019).

We determined the solar photospheric present-day Z/X ratio of 0.0225, when calculated using the photospheric abundances only, and 0.0226, when the meteoritic abundances were used for most species, except C, N, and O, for which the photospheric values are used. Our estimates are 26% higher compared to those determined by Asplund et al. (2021), but they are in a much better agreement with Caffau et al. (2011) and Grevesse & Sauval (1998), the difference being 10% and 1%, respectively. Very close numerical agreement of Z/X with Grevesse & Sauval (1998) is, however, fortuitous, as abundances of individual elements are different in their study and our own. While the latter study made use of 1D LTE models, their uncertainties are more conservative (on the order of 10–20% for most elements) and appear to be more realistic, which accounts for the difference with Asplund et al. (2009, 2021).

Our detailed calculations of SSMs suggest that the chemical composition presented in this study leads to consistent results between the interior structure of the Sun and the helioseismic quantities that match the results based on the old spectroscopic results (e.g. Grevesse & Noels 1993; Grevesse & Sauval 1998). It is the first time that SSMs using state-of-the-art spectroscopic results for solar abundances are able to reproduce the solar interior properties determined through helioseismic techniques. We are confident this works brings us close to a solution of the so-called solar abundance problem, which arose in the early 2000s in light of the initial results on solar O based on 3D models and NLTE line formation (Asplund 2005). It is a problem that has defied all attempted solutions in the form of non-standard stellar physics. Any residual differences can possibly be explained by other systematic limitations on stellar models (Buldgen et al. 2019).

Acknowledgements. We acknowledge support by the Collaborative Research centre SFB 881 (projects A4, A5, A10), Heidelberg University, of the Deutsche Forschungsgemeinschaft (DFG, German Research Foundation). M.B. is supported through the Lise Meitner grant from the Max Planck Society. A.S. is supported by the MICINN grant PRPPID2019-108709GB-I00 and the European Union's Horizon 2020 research and innovation programme under grant agreement No. 101008324 (ChETEC-INFRA) and by the Spanish program Unidad de Excelencia Maria de Maeztu CEX2020-001058-M. B.P. is supported in part by The Centre National d'Etudes Spatiales (CNES). This project has received funding from the European Research Council (ERC) under the European Union's Horizon 2020 research and innovation programme (Grant agreement No. 949173). U.H. acknowledges support from the Swedish National Space Agency (SNSA/Rymdstyrelsen). We thank Henrik Hartman for providing new atomic data for Si transitions. E.M. would like to thank Richard Hoppe for many productive discussions. We thank an anonymous referee for their helpful suggestions and comments.

References

Adibekyan, V. 2019, Geosciences, 9, 105
Alexeeva, S. A., & Mashonkina, L. I. 2015, MNRAS, 453, 1619
Alexeeva, S., Ryabchikova, T., Mashonkina, L., & Hu, S. 2018, ApJ, 866, 153
Alexeeva, S., Chen, T., Ryabchikova, T., et al. 2020, ApJ, 896, 59
Amarsi, A. M., & Asplund, M. 2017, MNRAS, 464, 264
Amarsi, A. M., Lind, K., Asplund, M., Barklem, P. S., & Collet, R. 2016, MNRAS, 463, 1518
Amarsi, A. M., Barklem, P. S., Asplund, M., Collet, R., & Zatsarinny, O. 2018, A&A, 616, A89
Amarsi, A. M., Barklem, P. S., Collet, R., Grevesse, N., & Asplund, M. 2019, A&A, 624, A111
Amarsi, A. M., Grevesse, N., Grumer, J., et al. 2020, A&A, 636, A120
Amarsi, A. M., Grevesse, N., Asplund, M., & Collet, R. 2021, A&A, 656, A113
Anders, E., & Grevesse, N. 1989, Geochim. Cosmochim. Acta, 53, 197
Anstee, S. D., & O'Mara, B. J. 1991, MNRAS, 253, 549
Anstee, S. D., & O'Mara, B. J. 1995, MNRAS, 276, 859
Asplund, M. 2005, ARA&A, 43, 481
Asplund, M., Grevesse, N., Sauval, A. J., & Scott, P. 2009, ARA&A, 47, 481
Asplund, M., Amarsi, A. M., & Grevesse, N. 2021, A&A, 653, A141
Badnell, N. R. 2011, in 7th International Conference on Atomic and Molecular Data and Their Applications – ICAMDATA-2010, eds. A. Bernotas, R. Karazija, & Z. Rudzikas, AIP Conf. Ser., 1344, 139

Badnell, N. R., Bautista, M. A., Butler, K., et al. 2005, MNRAS, 360, 458
Bahcall, J. N., Serenelli, A. M., & Basu, S. 2005, ApJ, 621, L85
Bailey, J. E., Nagayama, T., Loisel, G. P., et al. 2015, Nature, 517, 56
Bard, A., & Kock, M. 1994, A&A, 282, 1014
Bard, A., Kock, A., & Kock, M. 1991, A&A, 248, 315
Barklem, P. S. 2018, A&A, 612, A90
Barklem, P. S., & Aspelund-Johansson, J. 2005, A&A, 435, 373
Barklem, P. S., Piskunov, N., & O'Mara, B. J. 2000, A&AS, 142, 467
Barklem, P. S., Belyaev, A. K., Spielfiedel, A., Guitou, M., & Feautrier, N. 2012, A&A, 541, A80
Basu, S. 2021, ApJ, 917, 45
Basu, S., & Antia, H. M. 1997, MNRAS, 287, 189
Basu, S., & Antia, H. M. 2008, Phys. Rep., 457, 217
Basu, S., Mazumdar, A., Antia, H. M., & Demarque, P. 2004, MNRAS, 350, 277
Basu, S., Chaplin, W. J., Elsworth, Y., New, R., & Serenelli, A. M. 2009, ApJ, 699, 1403
Bautista, M. A., Lind, K., & Bergemann, M. 2017, A&A, 606, A127
Bedell, M., Bean, J. L., Meléndez, J., et al. 2018, ApJ, 865, 68
Belyaev, A. K., Yakovleva, S. A., & Barklem, P. S. 2014, A&A, 572, A103
Belyaev, A. K., Voronov, Y. V., Mitrushchenkov, A., Guitou, M., & Feautrier, N. 2019, MNRAS, 487, 5097
Bensby, T., Feltzing, S., & Oey, M. S. 2014, A&A, 562, A71
Bergemann, M. 2011, MNRAS, 413, 2184
Bergemann, M., & Cescutti, G. 2010, A&A, 522, A9
Bergemann, M., & Nordlander, T. 2014, ArXiv e-prints [arXiv:1403.3088]
Bergemann, M., Pickering, J. C., & Gehren, T. 2010, MNRAS, 401, 1334
Bergemann, M., Lind, K., Collet, R., Magic, Z., & Asplund, M. 2012, MNRAS, 427, 27
Bergemann, M., Kudritzki, R.-P., Würl, M., et al. 2013, ApJ, 764, 115
Bergemann, M., Collet, R., Amarsi, A. M., et al. 2017, ApJ, 847, 15
Bergemann, M., Sesar, B., Cohen, J. G., et al. 2018, Nature, 555, 334
Bergemann, M., Gallagher, A. J., Eitner, P., et al. 2019, A&A, 631, A80
Bergemann, M., Hoppe, R., Semenova, E., et al. 2021, MNRAS, 508, 2236
Berrington, K. A., Eissner, W. B., & Norrington, P. H. 1995, Comput. Phys. Commun., 92, 290
Blackwell, D. E., Petford, A. D., Shallis, M. J., & Simmons, G. J. 1982a, MNRAS, 199, 43
Blackwell, D. E., Petford, A. D., & Simmons, G. J. 1982b, MNRAS, 201, 595
Bochsler, P. 2007, A&A, 471, 315
Breitschwerdt, D., & de Avillez, M. A. 2021, Ap&SS, 366, 94
Buder, S., Sharma, S., Kos, J., et al. 2021, MNRAS, 506, 150
Buldgen, G., Salmon, S. J. A. J., Noels, A., et al. 2019, A&A, 621, A33
Caffau, E., Faraggiana, R., Bonifacio, P., Ludwig, H. G., & Steffen, M. 2007, A&A, 470, 699
Caffau, E., Ludwig, H. G., Steffen, M., et al. 2008, A&A, 488, 1031
Caffau, E., Ludwig, H. G., Bonifacio, P., et al. 2010, A&A, 514, A92
Caffau, E., Ludwig, H. G., Steffen, M., Freytag, B., & Bonifacio, P. 2011, Sol. Phys., 268, 255
Caffau, E., Ludwig, H. G., Malherbe, J. M., et al. 2013, A&A, 554, A126
Carlsson, M. 1986, Upps. Astron. Obs. Rep., 33
Civiš, S., Kubelík, P., Ferus, M., et al. 2018, ApJS, 239, 11
Cowan, R. D. 1981, The Theory of Atomic Structure and Spectra (Berkeley: University of California Press)
Deal, M., Goupil, M. J., Marques, J. P., Reese, D. R., & Lebreton, Y. 2020, A&A, 633, A23
Den Hartog, E. A., Lawler, J. E., Sneden, C., et al. 2021, ApJS, 255, 27
Drake, J. J., & Testa, P. 2005, Nature, 436, 525
Drawin, H.-W. 1968, Z. Phys., 211, 404
Ferguson, J. W., Alexander, D. R., Allard, F., et al. 2005, ApJ, 623, 585
Freytag, B., Steffen, M., Ludwig, H.-G., et al. 2012, J. Comput. Phys., 231, 919
Froese Fischer, C., Godefroid, M., Brage, T., Jönsson, P., & Gaigalas, G. 2016, J. Phys. B At. Mol. Opt. Phys., 49, 182004
Froese Fischer, C., Gaigalas, G., Jönsson, P., & Bieroń, J. 2019, Comput. Phys. Commun., 237, 184
Fuhr, J. R., Martin, G. A., & Wiese, W. L. 1988, J. Physical and Chemical Reference Data, 17
Gallagher, A. J., Bergemann, M., Collet, R., et al. 2020, A&A, 634, A55
Garz, T. 1973, A&A, 26, 471
Gehren, T., Liang, Y. C., Shi, J. R., Zhang, H. W., & Zhao, G. 2004, A&A, 413, 1045
Geiss, J., Buehler, F., Cerutti, H., & Eberhardt, P. 1972, Solar-Wind Composition Experiment (Washington: NASA), 289, 15
Gloeckler, G., & Fisk, L. A. 2007, Space Sci. Rev., 130, 489
Grant, I. 2007, Relativistic Quantum Theory of Atoms and Molecules: Theory and Computation, Springer Series on Atomic, Optical, and Plasma Physics (New York: Springer)
Grevesse, N., & Noels, A. 1993, in Origin and Evolution of the Elements, eds. N. Prantzos, E. Vangioni-Flam, & M. Casse, 15
Grevesse, N., & Sauval, A. J. 1998, Space Sci. Rev., 85, 161
Gustafsson, B., Edvardsson, B., Eriksson, K., et al. 2008, A&A, 486, 951
Guzik, J. A., & Mussack, K. 2010, ApJ, 713, 1108
Heiter, U., Lind, K., Bergemann, M., et al. 2021, A&A, 645, A106
Henyey, L., Vardya, M. S., & Bodenheimer, P. 1965, ApJ, 142, 841
Hibbert, A., Biemont, E., Godefroid, M., & Vaeck, N. 1991, J. Phys. B At. Mol. Phys., 24, 3943
Hibbert, A., Biemont, E., Godefroid, M., & Vaeck, N. 1993, A&AS, 99, 179
Johansson, S., Litzén, U., Lundberg, H., & Zhang, Z. 2003, ApJ, 584, L107
Johnson, W., Kolb, D., & Huang, K.-N. 1983, At. Data Nucl. Data Tab., 28, 333
Jönsson, P., & Godefroid, M. R. 2000, Mol. Phys., 98, 1141
Juett, A. M., Schulz, N. S., Chakrabarty, D., & Gorczyca, T. W. 2006, ApJ, 648, 1066
Korotin, S. A. 2009, Astron. Rep., 53, 651
Korotin, S., Andrievsky, S., Caffau, E., & Bonifacio, P. 2017, in Stars: From Collapse to Collapse, eds. Y. Y. Balega, D. O. Kudryavtsev, I. I. Romanyuk, & I. A. Yakunin, ASP Conf. Ser., 510, 141
Laming, J. M., Heber, V. S., Burnett, D. S., et al. 2017, ApJ, 851, L12
Lawler, J. E., Hala, Sneden, C., et al. 2019, ApJS, 241, 21
Li, W., Amarsi, A. M., Papoulia, A., Ekman, J., & Jönsson, P. 2021, MNRAS, 502, 3780
Lind, K., Bergemann, M., & Asplund, M. 2012, MNRAS, 427, 50
Lind, K., Amarsi, A. M., Asplund, M., et al. 2017, MNRAS, 468, 4311
Lodders, K. 2003, ApJ, 591, 1220
Lodders, K. 2019, ArXiv e-prints [arXiv:1912.00844]
Lodders, K. 2021, Space Sci. Rev., 217, 44
Ludwig, H.-G., Caffau, E., Steffen, M., et al. 2009, Mem. Soc. Astron. It., 80, 711
Magic, Z., Collet, R., Asplund, M., et al. 2013a, A&A, 557, A26
Magic, Z., Collet, R., Hayek, W., & Asplund, M. 2013b, A&A, 560, A8
Maiorca, E., Uitenbroek, H., Uttenthaler, S., et al. 2014, ApJ, 788, 149
Majewski, S. R., Schiavon, R. P., Frinchaboy, P. M., et al. 2017, AJ, 154, 94
Mashonkina, L. 2013, A&A, 550, A28
Mashonkina, L. 2020, MNRAS, 493, 6095
Mashonkina, L., Sitnova, T., & Belyaev, A. K. 2017, A&A, 605, A53
Mashonkina, L., Sitnova, T., Yakovleva, S. A., & Belyaev, A. K. 2019, A&A, 631, A43
Mauas, P. J., Avrett, E. H., & Loeser, R. 1988, ApJ, 330, 1008
May, M., Richter, J., & Wichelmann, J. 1974, A&AS, 18, 405
Meléndez, J., & Barbuy, B. 2009, A&A, 497, 611
Meyer, J. P. 1989, in Cosmic Abundances of Matter, ed. C. J. Waddington, AIP Conf. Ser., 183, 245
Nieva, M. F., & Przybilla, N. 2012, A&A, 539, A143
Nieva, M. F., & Simón-Díaz, S. 2011, A&A, 532, A2
Nissen, P. E., Silva Aguirre, V., Christensen-Dalsgaard, J., et al. 2017, A&A, 608, A112
Nordlander, T., & Lind, K. 2017, A&A, 607, A75
O'Brian, T. R., & Lawler, J. E. 1991, Phys. Rev. A, 44, 7134
O'Brian, T. R., Wickliffe, M. E., Lawler, J. E., Whaling, W., & Brault, J. W. 1991, J. Opt. Soc. Am. B Opt. Phys., 8, 1185
Osorio, Y., Barklem, P. S., Lind, K., et al. 2015, A&A, 579, A53
Osorio, Y., Lind, K., Barklem, P. S., Allende Prieto, C., & Zatsarinny, O. 2019, A&A, 623, A103
Palme, H., Lodders, K., & Jones, A. 2014, in Solar System Abundances of the Elements, ed. A. M. Davis, 2, 15
Park, J., Kucharek, H., Möbius, E., et al. 2014, ApJ, 795, 97
Pehlivan Rhodin, A., Hartman, H., Nilsson, H., & Jönsson, P. 2017, A&A, 598, A102
Pinsonneault, M. H., & Delahaye, F. 2009, ApJ, 704, 1174
Piskunov, N. E., Kupka, F., Ryabchikova, T. A., Weiss, W. W., & Jeffery, C. S. 1995, A&AS, 112, 525
Plez, B. 2012, Astrophysics Source Code Library [record ascl:1205.004]
Quinet, P., Palmeri, P., Biémont, E., et al. 1999, MNRAS, 307, 934
Quinet, P., Palmeri, P., Biémont, E., et al. 2002, J. Alloy. Compd., 344, 255
Raassen, A. J. J., & Uylings, P. H. M. 1998, A&A, 340, 300
Reames, D. V. 1998, Space Sci. Rev., 85, 327
Reggiani, H., Amarsi, A. M., Lind, K., et al. 2019, A&A, 627, A177
Reiners, A., Mrotzek, N., Lemke, U., Hinrichs, J., & Reinsch, K. 2016, A&A, 587, A65
Ruffoni, M. P., Den Hartog, E. A., Lawler, J. E., et al. 2014, MNRAS, 441, 3127
Ryabchikova, T., Piskunov, N., Kurucz, R. L., et al. 2015, Phys. Scr., 90, 054005
Schuler, S. C., Andrews, J. J., Clanzy, V. R., et al. 2021, AJ, 162, 109
Scott, P., Grevesse, N., Asplund, M., et al. 2015a, A&A, 573, A25
Scott, P., Asplund, M., Grevesse, N., Bergemann, M., & Sauval, A. J. 2015b, A&A, 573, A26
Seaton, M. J. 1962, in Atomic and Molecular Processes, ed. D. R. Bates, 375
Semenova, E., Bergemann, M., Deal, M., et al. 2020, A&A, 643, A164

Serenelli, A. M., Basu, S., Ferguson, J. W., & Asplund, M. 2009, ApJ, 705, L123
Serenelli, A. M., Haxton, W. C., & Peña-Garay, C. 2011, ApJ, 743, 24
Shi, J. R., Gehren, T., Butler, K., Mashonkina, L. I., & Zhao, G. 2008, A&A, 486, 303
Sitnova, T., Zhao, G., Mashonkina, L., et al. 2015, ApJ, 808, 148
Smiljanic, R., Korn, A. J., Bergemann, M., et al. 2014, A&A, 570, A122
Smith, G. 1988, J. Phys. B At. Mol. Phys., 21, 2827
Smith, G., & Raggett, D. S. J. 1981, J. Phys. B At. Mol. Phys., 14, 4015
Steinmetz, M., Guiglion, G., McMillan, P. J., et al. 2020, AJ, 160, 83
Storey, P. J., & Zeippen, C. J. 2000, MNRAS, 312, 813
Takeda, Y., Hashimoto, O., Taguchi, H., et al. 2005, PASJ, 57, 751
The Opacity Project Team 1995, The Opacity Project (Bristol, UK: Institute of Physics Publications)
Tremblay, P.-E., Ludwig, H.-G., Freytag, B., Steffen, M., & Caffau, E. 2013, A&A, 557, A7
Uitenbroek, H., & Criscuoli, S. 2011, ApJ, 736, 69
Unsöld, A. 1955, Physik der Sternatmospharen, MIT Besonderer Berucksichtigung der Sonne (Berlin: Springer)
van Regemorter, H. 1962, ApJ, 136, 906
Villante, F. L., Serenelli, A. M., Delahaye, F., & Pinsonneault, M. H. 2014, ApJ, 787, 13
Vincent, A. C., Scott, P., & Serenelli, A. 2015, Phys. Rev. Lett., 114, 081302
Vinyoles, N., Serenelli, A. M., Villante, F. L., et al. 2017, ApJ, 835, 202
Weiss, A., & Schlattl, H. 2008, Ap&SS, 316, 99
Widing, K. G. 1997, ApJ, 480, 400
Wolnik, S. J., Berthel, R. O., & Wares, G. W. 1971, ApJ, 166, L31
Wood, M. P., Lawler, J. E., Sneden, C., & Cowan, J. J. 2014, ApJS, 211, 20
Young, P. R. 2005, A&A, 444, L45
Young, P. R. 2018, ApJ, 855, 15
Zhang, H. W., Butler, K., Gehren, T., Shi, J. R., & Zhao, G. 2006, A&A, 453, 723
Zhao, G., Butler, K., & Gehren, T. 1998, A&A, 333, 219
Zhao, G., Mashonkina, L., Yan, H. L., et al. 2016, ApJ, 833, 225

Appendix A: Appendix

Herem we provide abundances derived from individual lines observed in the solar spectrum. Details on these methods are given in Sect. 2.

Table A.1. ⟨3D⟩ NLTE abundances derived from individual spectral lines.

λ [Å]	A(el)	λ [Å]	A(El)
C I		Fe I	
5052.160	8.61	5242.491	7.52
6587.610	8.51	5365.399	7.17
7113.180	8.57	5379.574	7.55
N I		5398.279	7.50
8629.200	8.05	5560.212	7.61
8683.400	7.91	5638.262	7.42
O I		5661.346	7.44
6300.304	8.75	5679.023	7.79
7771.940	8.76	5731.762	7.69
7774.170	8.78	5741.848	7.63
7775.390	8.79	5855.077	7.49
Mg I		5905.672	7.49
5528.405	7.51	5930.180	7.63
5711.088	7.59	6027.051	7.51
Si I		6056.005	7.41
5645.600	7.60	6093.644	7.65
5684.480	7.60	6165.360	7.56
5690.425	7.62	6187.990	7.53
5701.104	7.52	6270.225	7.47
5772.146	7.62	Fe II	
5793.073	7.49	5234.625	7.39
6741.640	7.71	5325.553	7.43
7034.900	7.69	5425.257	7.45
7226.210	7.58	5543.936	7.55
Ca I		6084.111	7.59
5260.387	6.30	6456.383	7.54
5512.980	6.35	Ni I	
5867.562	6.42	4740.170	6.26
6166.439	6.38	4811.980	6.26
6455.598	6.37	4814.600	6.19
6471.662	6.35	4976.130	6.20
6499.650	6.39	5157.980	6.13
		5537.100	6.07
		6176.820	6.29
		6204.600	6.24
		6223.990	6.23
		6414.590	6.24
		Ni II	
		6378.260	6.26